Thesis for the degree of Licentiate of Engineering

Tilted Foils Nuclear Spin Polarization and Measurement with Coulomb Excitation

Hans T. Törnqvist

Department of Fundamental Physics
Chalmers University of Technology
Göteborg, Sweden 2012

Tilted Foils Nuclear Spin Polarization and Measurement with Coulomb Excitation

Hans T. Törnqvist

Department of Fundamental Physics
Chalmers University of Technology
SE-412 96 Göteborg
Sweden
Telephone: +46 (0)31-772 10 00

Chalmers Reproservice
Göteborg, Sweden 2012

Tilted Foils Nuclear Spin Polarization and Measurement with Coulomb Excitation

Hans T. Törnqvist
Department of Fundamental Physics
Chalmers University of Technology

Abstract

Developing new experimental tools is essential to expand the possibilites of probing the structure of atomic nuclei. The better the currently known properties of nuclei can be manipulated, the more information can be extracted from data collected in nuclear reaction experiments. One property that has been controlled for many years is the nuclear spin, but this has only been viable for a certain set of isotopes with restrictions on for example specific atomic excitation schemes or half-lives.

This thesis will provide details on an evaluation project using thin tilted foils after the REX-ISOLDE linac at the CERN-ISOLDE experimental facility, to polarize the spin of nuclei in-flight. The nuclear polarization is then measured with a technique based on Coulomb excitation, which is a flexible and readily available experimental method at ISOLDE with the MINIBALL spectrometer. The tilted foils technique may be beneficial to polarize the nuclear spin of short-lived radioactive beams that can be difficult by other means. The only restrictions on the accelerated ions known so far to produce polarization with tilted foils are non-zero nuclear and atomic spin.

The β-NMR is an alternative, more common technique for measuring nuclear spin polarization. No such setup connected to REX-ISOLDE existed at the start of the project which prompted for the Coulomb excitation method with MINIBALL. Although, a β-NMR setup is currently under construction and testing.

Keywords:
Nuclear Spin Polarization, Tilted Foils, Coulomb Excitation

Contents

Chapter 1

Introduction

1.1 Motivation for the use of polarized beams

As the research into the structure of the nucleus progresses, novel techniques and apparatus need to be developed. One possible direction of progress is to control certain properties of nuclei in an experiment to increase the available information content. Currently, many properties of the exotic nuclei in beams produced at radioactive beam facilities are left undetermined, the nuclear spin being one such property addressed in this project. By introducing non-uniform state populations in ensembles of nuclei, reaction or decay channels which are related to the fixed nuclear state could be further examined. Examples of such studies include the determination of g-factors of nuclear ground states and long-lived isomeric states, studies of the nuclear quadrupole moments, or investigations of parity non-conservation in nuclei.

The polarization techniques in use today aim for high degrees of polarization, but suffer restrictions on the final beam energy, life times or atomic decay schemes. One of them relies on resonant excitations of atomic transitions with circularly polarized light, so-called optical pumping. To use it, a suitable transition needs to exist and be accessible with available laser sys-

tems. Another method is based on spin polarization via sub-K temperatures. It can be applied to many isotopes, but the beam has to be stopped to be polarized. Finally, at fragmentation facilities, at certain angles the fragmented beams can be polarized in the production reaction. Depending on the experiment, the proper polarization technique needs to be chosen, and for some isotopes present techniques are not ideal.

This project took place at the CERN-ISOLDE facility and aimed at evaluating a fast and versatile in-flight polarization technique using foils tilted at an oblique angle with respect to the beam direction. Because the introduction of foils in a beam line is relatively non-destructive, this technique could be appropriate for beam post-acceleration up to energies of several MeV/u. In principle, the only restriction is non-zero atomic and nuclear spins of the accelerated ions, making it a very universal approach. The potential to access polarized beams in the MeV energy domain is interesting for Coulomb excitation and transfer reaction experiments, in order to extend the currently available methods to probe nuclear structure. The tilted foils may also allow polarized beams of many exotic isotopes at lower energies to extend applications to other fields of experimental physics, such as solid-state- and bio-physics [1].

1.2 ISOLDE

The ISOLDE [2] facility at CERN is at the forefront of ISotope OnLine (ISOL) separator facilities. Since the start of operation, pure beams of more than 700 isotopes from over 70 of the elements with currents up to 10^{10} ions/s have been delivered by ISOLDE [3]. The available isotopes over the nuclear chart can be seen in Figure 1.1. The flexible design of the facility allows for a wide range of beam energies and experiments, from keV/u for decay studies, mass spectrometry, laser spectroscopy, solid-state- and bio-physics, up to the MeV/u-region for Coulomb excitation and nucleon transfer experiments.

Because this project has so far used a beam of stable ions, only a very brief introduction to the production of radioactive isotopes will be given. Exotic

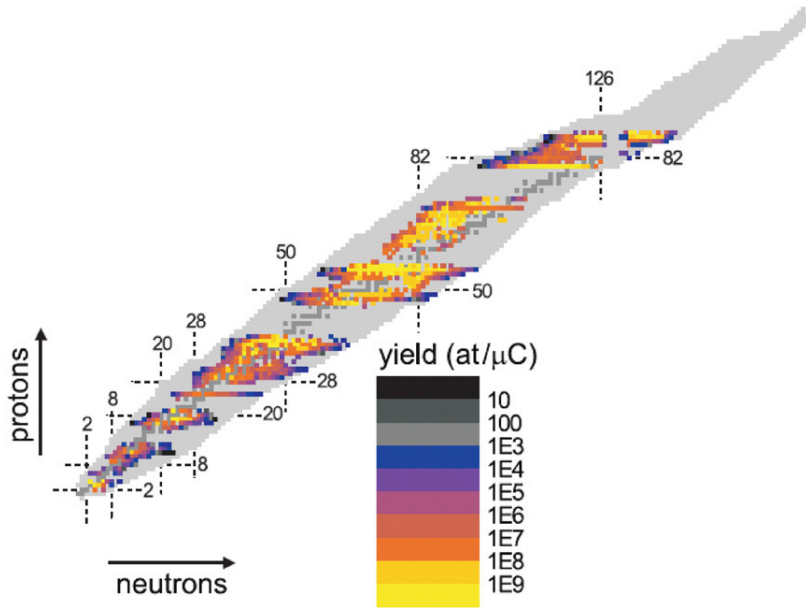

Figure 1.1: Yields of isotopes successfully produced and extracted at the ISOLDE facility. Picture taken from [4].

nuclei are produced at ISOL facilities via spallation, fission or fragmentation reactions in thick targets after bombardment of high-intensity beams of high-energy light particles. In the case of ISOLDE the beam particles are protons, which are accelerated in the PS Booster circular accelerator to an energy of 1.4 GeV and are ejected in pulses of up to $3 \cdot 10^{13}$ protons every 1.2 s or its multiples. On average, the target receives a current of up to 2 µA of protons. At ISOLDE, there are two target and separator setups, namely the General Purpose Separator (GPS) and the High Resolution Separator (HRS). To assure fast extraction of the produced radioactive isotopes, the targets generally are porous and heated electrically to 1500–2000°C for fast diffusion of the created atoms. The atoms diffuse further via a heated transfer line, after which they undergo ionization to $q = +1$ and are accelerated by a $30 - -60$ keV static electric potential. With this method, isotopes with half lifes down to a few

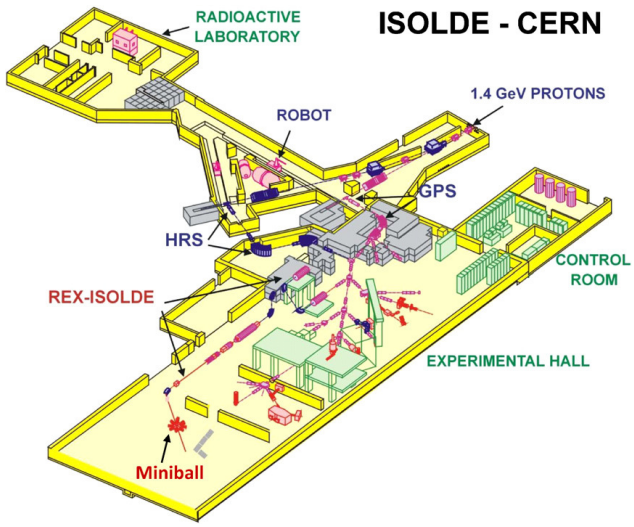

Figure 1.2: Schematic overview of the ISOLDE hall. The high-energy beams are available only after the REX-ISOLDE linac, the remaining space is devoted to low-energy beams. From [4].

milliseconds have been extracted and used for studies.

Polarized beams are routinely produced in the low-energy domains. Two experimental setups located at ISOLDE are COLLAPS, that utilizes optical pumping with circularly polarized lasers [5], and NICOLE based on low temperature orientation close to absolute zero temperatures [6]. Optical pumping can produce degrees of polarizations up to almost 100% for certain isotopes, but is otherwise restricted by specific laser excitation schemes. Low temperature orientation requires catching or trapping and cooling of nuclei down to temperatures less than 1 K depending on the isotope and implantation host.

1.2.1 REX-ISOLDE

Experiments in the low-energy domain were the staple of ISOLDE operation for approximately 30 years. In 1994, the linear accelerator REX-ISOLDE was proposed for post-acceleration of ISOLDE beams and it became operational in

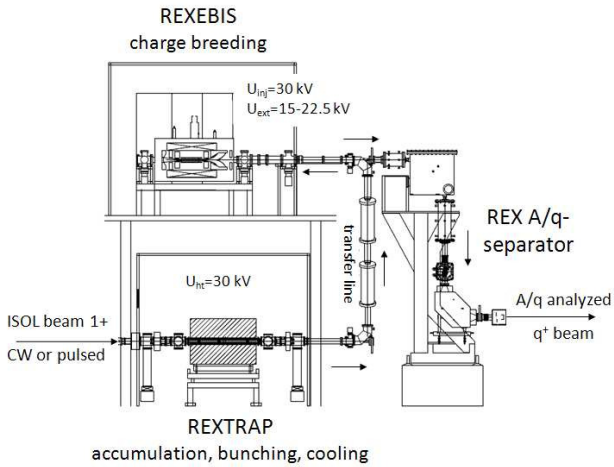

Figure 1.3: Schematic drawing of REX-ISOLDE ion preparation stage including REX-TRAP and REX-EBIS. Picture taken from [7].

2001. The accelerating cavities occupy a length of 10 m and have successfully accelerated more than 90 radioactive isotopes up to energies of 3.0 MeV/u with good experimental yields [4]. The following sections will treat the major components involved in preparing singly ionized low-energy radioactive beams for post-acceleration to intermediate energies for experiments.

Cooling and bunching in REX-TRAP

Following ionization and extraction from the online ion source, the beam possesses a high transversal emittance which makes injection into the charge breeder inefficient. Therefore, the beam is cooled transversally in the REX-TRAP Penning trap [8]. A high voltage electric potential and a static magnetic solenoid field are used to confine the trapped ions and an inert buffer gas cools the ions. The electrical confinement field and the buffer gas are schematically illustrated in Figure 1.4. The electric potential decelerates the ions into a trapping region with an axially quadratic potential well, whereas the static magnetic field constrains the radial movement of the ions. The inert buffer

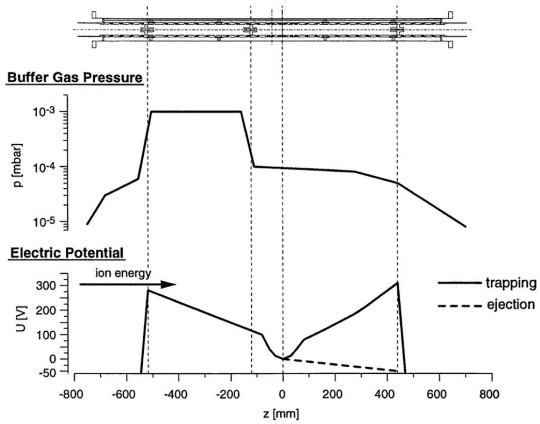

Figure 1.4: Illustration of the buffer gas and electric trapping field in REX-TRAP. In the electric potential diagram, the solid line describes the trapping potential and the dashed line the potential at ejection of the cooled ions. From [8].

gas, Ar or Ne, cools down the ions via energy dissipation from collisions. After a few ms, the electric field at the exit side of the trap is rapidly lowered below the kinetic energy of the cooled ions, which escape in a short bunch. The temporal width of one bunch is approximately 10–50 µs. At the exit, the ions are re-accelerated to 30 keV and travel to REX-EBIS for charge breeding.

Charge breeding in REX-EBIS

The accelerating cavities in the linac increase the beam energy by employing radio frequency (RF) fields interacting with the charge of the ions. Singly charged ions present a small charge-to-mass ratio which requires a high accelerating voltage, resulting in a long accelerator, for adequate acceleration. To avoid this, the solution implemented at REX-ISOLDE is to decrease the charge-to-mass ratio (A/q) by charge breeding before the acceleration stages. REX-EBIS [7, 9] has successfully produced many beams with A/q between 2.5 and 4.5. Internally, REX-EBIS has a design similar to REX-TRAP, but the buffer gas profile is replaced with an electron beam operating in Ultra High

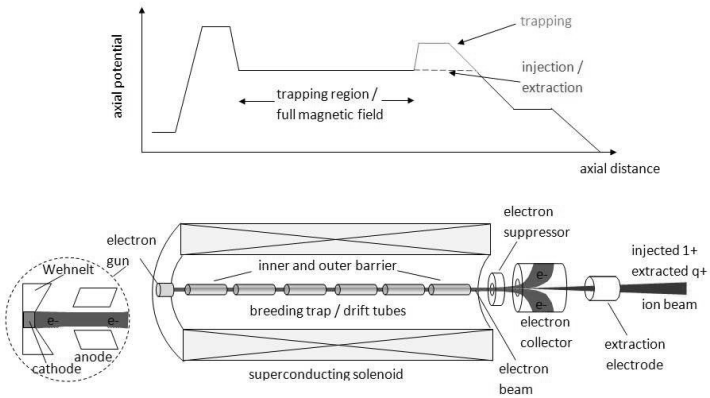

Figure 1.5: Illustration of key components inside REX-EBIS, such as the the trapping magnetic field and the electron beam. The meaning of the solid and dashed lines in the electric potential diagram are similar to Figure 1.4. From [7].

Vacuum (UHV) of at least 10^{-11} mbar. The electron gun shoots high intensity, highly energetic electrons onto the trapped ions that strip away atomic electrons from the trapped ions. After charge-breeding, the ions are ejected by lowering the trapping field and they enter a mass separator which selects the desired A/q. The charge-bred ions are then transported to the linear accelerator cavities and beam focusing elements.

It should be noted that REX-TRAP and REX-EBIS may run in offline mode without beams delivered by the ISOLDE separators by injecting gas directly into REX-EBIS and therein producing the highly charged ions. This is especially useful for stable isotopes in order to provide an easily controllable high intensity beam.

Accelerating cavities and beam focusing

As has been mentioned, the REX-ISOLDE accelerating cavities [10] operate with RF fields. The acceleration is performed step-wise by six separate devices: the RFQ, IHS, three so-called 7-gaps and 9-gap resonating cavities. The acceleration energy cannot be configured with continuous resolution over the full energy range, but a fixed set of energies can be attained by activating only some of the cavities. The lowest and highest possible beam energies are currently 298 keV/u and 3.0 MeV/u, respectively. During transport between the cavities and up to experimental setups, pairs or triplets of quadrupole magnets in alternating orientation around the beam provide focusing of the accelerated ions.

Chapter 2

Theory

2.1 Formal treatment of nuclear spin polarization

In order to determine the relationship between spin polarization and the effects in nuclear reactions, a formal introduction to polarization is given below. For further details, see [11, 12] on which this section is based.

The polarization of J of a spin system refers to the distribution of the spin projection J_z against a chosen polarization axis z. The amount of polarization can be written as:

$$p_J = \frac{1}{\hbar} \frac{\langle J_z \rangle}{\sqrt{J(J+1)}}$$

From here on, J will denote atomic spin and I nuclear spin.

Maximum polarization of an ensemble of nuclei implies that all the nuclei possess the largest possible spin projection against the polarization axis z. Under rotation around the z axis, the total spin of the ensemble should be

invariant. In terms of the density matrix ρ over spin states, letting:

$$\rho = D_z \, \rho \, D_z^{\dagger} \tag{2.1}$$

where D_z is a rotation operator defining a rotation around the z axis, it can be shown that ρ must be diagonal. When describing nuclear orientation, the density matrix formalism is readily replaced by irreducible statistical tensors which can be directly related to the density matrix:

$$t_{kq} = \hat{s} \sum_{\mu\mu'} (-1)^{s-\mu} \langle ss; \mu' - \mu | kq \rangle \rho_{\mu\mu'} \tag{2.2}$$

$$\rho_{\mu\mu'} = \frac{1}{\hat{s}} \sum_{kq} (-1)^{s-\mu} \langle ss; \mu' - \mu | kq \rangle t_{kq} \tag{2.3}$$

where s is the spin of the particle under consideration, $\hat{s} = \sqrt{2s+1}$ and k ($-s \leq k \leq s$) is called the *rank* of the statistical tensor. The factors $\langle ss; \mu' - \mu | kq \rangle$ are the Clebsch-Gordan coefficients (CGC). The main reason for introducing the irreducible statistical tensors is the simpler transformation properties. For example, choosing an integer or half-integer spin s, the set of tensors $t_{(k=s)q}$ are rotationally independent from $t_{(k\neq s)q}$, whereas the diagonal terms in the density matrix formalism are mixed under rotation. Also, the expression of t_{00} simplifies to the expectation value of the unit operator, thus $t_{00} = 1$ for normalized states.

In the literature, the Wigner 3j-symbol is a common alternative to express statistical tensors. The relationship between CGCs and the Wigner 3j-symbol is:

$$\langle j_1 j_2; m_1 m_2 | j_1 j_2; jm \rangle = (-1)^{j_1 - j_2 + m} \sqrt{2j+1} \begin{pmatrix} j_1 & j_2 & j \\ m_1 & m_2 & -m \end{pmatrix} \tag{2.4}$$

so that the irreducible statistical tensors, as written in this report, take the

form:

$$t_{kq} = \hat{s} \sum_{\mu\mu'} (-1)^{s-\mu+q} \sqrt{2k+1} \begin{pmatrix} s & s & k \\ \mu' & -\mu & -q \end{pmatrix} \rho_{\mu\mu'} \tag{2.5}$$

In terms of the irreducible statistical tensors, the polarization can be described by inserting Equation 2.3 in 2.1. Because the density matrix must be diagonal, any CGCs for $\mu \neq \mu'$ must be zeroed by t_{kq}. Following the notation in Equation 2.2, CGCs are in general non-zero only for $q = \mu - \mu'$, and thus:

$$t_{kq} = 0 \text{ for } q \neq 0 \tag{2.6}$$

In a scattering reaction with conserved parity, there will be a symmetry plane coplanar to the trajectory of the scattered particle. Let the normal of this plane be y, let z be parallel with the momentum of the incoming particle prior to the reaction and let x be perpendicular to both y and z, all three forming an orthogonal right-handed coordinate system. This coordinate system is normally referred to as the helicity frame. A reflection can be performed by a full parity operation and a rotation by π around y which is parallel with the normal of the reflection plane. The CGCs are invariant to the parity operation, and the rotation operator for an angle π around the y axis for CGCs can be written as:

$$d^k_{mm'}(\theta) = (-1)^{k-m} \ \delta_{m-m'}$$

The parity and rotation operations together give a second constraint on the statistical tensors for a polarized spin system in a scattering reaction with conserved parity:

$$t_{kq} = (-1)^{k+q} \ t_{k-q} \tag{2.7}$$

The final detection in an experiment is not dependent only on the particles under observation but also the detection system. The efficiency of the

detectors can be expressed also with the statistical tensors as T_{kq} and is referred to as the *analyzing power*. Given the counting rates $w = w(t_{kq})$ in an experiment, the analyzing power is defined as:

$$w(t_{kq}) \quad = \quad N \sum_{kq} t_{kq} T^*_{kq}$$

where N is a normalization coefficient, or in terms of reaction cross section:

$$\left(\frac{d\sigma}{d\Omega}\right)_{pol} \quad = \quad \left(\frac{d\sigma}{d\Omega}\right)_0 \sum_{kq} t_{kq} T^*_{kq} \tag{2.8}$$

where $\left(\frac{d\sigma}{d\Omega}\right)_{pol}$ and $\left(\frac{d\sigma}{d\Omega}\right)_0$ are the cross sections for a polarized and an unpolarized incoming particle, respectively. Because the cross section must be real and scalar under rotations for t_{kq}, the analyzing powers must obey the same two rules 2.6 and 2.7 as t_{kq}.

To conclude this section, the effect from scattering of particles with spin 1/2 will be shown. In this case, the spherical tensors can be readily written in terms of Cartesian tensors, which in the helicity frame are:

$$\begin{aligned}
\mathbf{p} &= \frac{1}{s}\mathrm{Tr}(\mathbf{s}\rho) \\
p_x &= -\frac{1}{\sqrt{2}}\left(t_{11} - t_{1-1}\right) \\
p_y &= \frac{i}{\sqrt{2}}\left(t_{11} + t_{1-1}\right) \\
p_z &= t_{10}
\end{aligned}$$

and similarly for the analyzing power $\mathbf{A} = (A_x, A_y, A_z)$ based on T_{kq}. From Equation 2.7, $p_x = p_z = A_x = A_z = 0$, so the polarization is directly related to p_y only in such reactions. Inserting the Cartesian tensors in Equation 2.8:

$$\left(\frac{d\sigma}{d\Omega}\right)_{pol} = \left(\frac{d\sigma}{d\Omega}\right)_0 (1 + \mathbf{p}\cdot\mathbf{A} + ...) = \left(\frac{d\sigma}{d\Omega}\right)_0 (1 + p_y A_y + ...)$$

where the omitted terms denote higher order tensor contributions from spin systems with spin higher than 1/2, and can be left out for this case. Assuming that a detector is placed to the "left" in the scattering plane, for example along the positive x axis in the helicity frame with y pointing up, the count rate of detections can be written:

$$L = N(1 + p_y A_y)$$

and the "right" side can be written following a rotation of the analyzing power by the angle π around the beam axis z:

$$\begin{aligned} A'_y &= -A_y \\ R &= N(1 - p_y A_y) \end{aligned}$$

Solving for the asymmetry measured in the detectors, the following accessible expression is obtained:

$$\frac{L - R}{L + R} = p_y A_y. \tag{2.9}$$

which shows that for a spin 1/2 particle the observed experimental scattering asymmetry is directly proportional to the nuclear polarization, with the analyzing power of the detector as the proportionality factor.

2.2 Spin polarization with the tilted foil method

As mentioned in the introduction section, nuclear spin polarization can be achieved by for example optical pumping with lasers or low-temperature orientation. Another common approach is to make use of fragmentation reactions. Here, we will describe in more detail how the nuclear spin polarization may be achieved when ions pass through thin foils tilted at oblique angles against the beam direction.

In short, at exit from a tilted foil the atoms or ions exhibit considerable

atomic polarization, which can be transferred to the nuclei in-flight via the hyperfine interaction. When using many foils, the nuclear polarization increases for every foil.

2.2.1 First studies

Interest in this method to polarize nuclear spins commenced in 1973, when two independent studies [13, 14] reported that a moving ion subject to any spatially asymmetric influence will induce a net atomic spin. The theory was based on studies of hyperfine quantum beats in the emission of gamma rays from ensembles of excited atoms. It was discovered that the quantum beats were related to the atomic spin orientation and alignment induced by a non-symmetric interaction around the beam. One way of achieving the broken symmetry was suggested with a foil oriented at an oblique angle against the beam direction. Experiments confirmed this with both transmission and reflection of the beam by observing circular polarization of photons emitted along the polarization axis.

One of the earliest reflection experiments was based on grazing incidence at angles $88 \pm 0.5°$ [15] and produced nuclear polarization at over 14 % for ^{14}N. Further experiments with the same isotope but with a reflection angle of 89.6° produced an atomic polarization of almost 23%. Reflection at such angles is very sensitive to the experimental geometry, ranging from large scale beam alignment down to the conditions close to and on the reflection surface. A vacuum pressure of at least 10^{-10} mbar was recommended to ensure little adsorption of contaminants. Furthermore, the energy exchange and heating due to the reflection may require cooling or restricted beam currents. Due to the experimental demands and complications of this type of experiment, especially the slight beam deviation which makes further post acceleration in an existing accelerator difficult, this technique was not considered for this project.

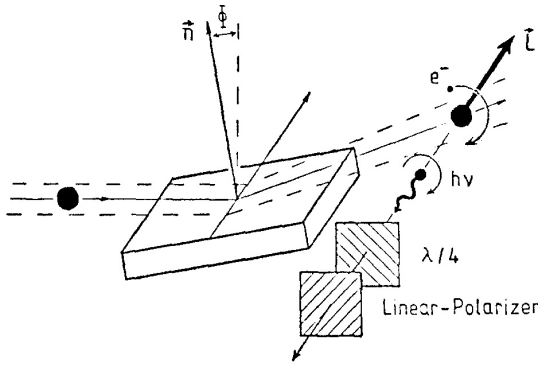

Figure 2.1: Grazing incidence on a copper plate to induce atomic polarization. The tilting angle Φ was at least $88 \pm 0.5°$ which required ultra clean conditions. Circular polarization of emitted photons was observed with a quarter wave plate and linear polarizer. From [16].

2.2.2 Atomic spin polarization

The mechanisms involved in atomic spin polarization via transmission through a foil have not been fully understood. Based on the theory of the asymmetric influence around the beam axis and results from early experiments, it has been suggested that the atomic spin projection is modified by a torque produced between the positively charged projectile ions and the atomic electrons in the foil [17]. This view of the process, pictured in Figure 2.2, coincides with the polarization direction that has been observed in experiments. When a projectile enters a foil, the atomic spin of the projectile is quickly destroyed by the symmetric distribution of charges inside the foil. At the exit, the atom will be subject to the asymmetric charge distribution at the surface and then traverse into vacuum with no external forces. Survey and derivations of the surface interactions taking into account many experimental observations have been published in [18, 19].

The atomic polarization is a strong function of the tilt angle and it has been shown that it reaches maximum at very large angles. For a purely vector-polarized system, the maximum vector polarization is $p_J = \frac{1}{3}\sqrt{\frac{J+1}{J}}$ and in

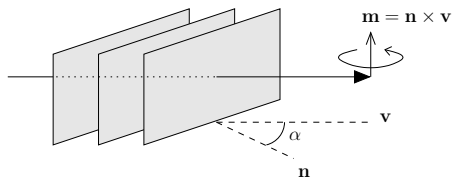

Figure 2.2: The direction of polarization coincides with a torque from the electric interaction between the positive projectiles and the electrons in the foil.

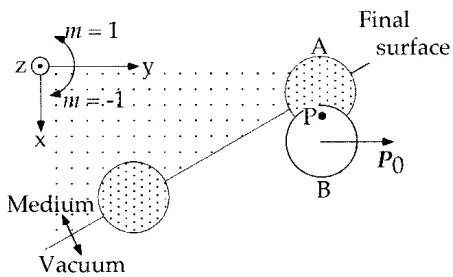

Figure 2.3: Schematic of interaction between a foil surface and a traveling ion, showing the momentum transfer. A is an atom in the foil at the exit surface, B is a passing ion with momenum P_0. From [17].

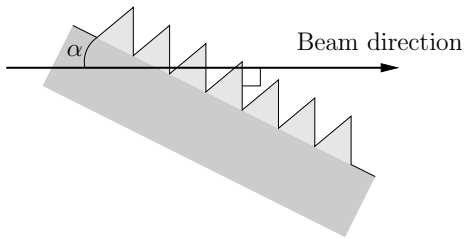

Figure 2.4: The worst case scenario of micro-structures at a foil surface tilted at an angle α to the beam direction, where the asymmetry of exit surface interactions are very small.

practice degrees of polarizations around 10% have been reported.

It is not known exactly how the surface roughness of foils impacts the efficiency of polarization, however grazing incidence experiments have shown that contaminants reduce the attained polarization. Rapidly reoccuring structures, such as in Figure 2.4, with large deviations in surface normals may give many exit surface normals almost parallel with the beam trajectory and can effectively reduce the asymmetry experienced by the exiting beam. The long range Coulomb interaction must be taken into account with arbitrary surface micro-structures, which makes it difficult to describe the process theoretically.

2.2.3 Transfer of atomic to nuclear spin polarization

As mentioned before, the polarization of atomic spin, taking place at the foil exit surface, is transferred to the nucleus via the hyperfine interaction during free flight in vacuum. In free space, the atomic spin J is not a good quantum number and it can be seen to oscillate if it has been polarized. This phenomenon is the hyperfine quantum beats. The reason for the oscillating behaviour is the coupling between J and I and that the good quantum number is the total spin $\mathbf{F} = \mathbf{I}+\mathbf{J}$. The transfer parameters $G^{qq'}_{kk'}(t)$ (note the difference in index notation to the previous section) as used in [20] between the atomic and nuclear spins can be integrated over time to give the time average spin projection of an ensemble of nuclei which is the value measured in experiments.

A depiction of the transfer in a classical view can be seen in Figure 2.5 (a-b).

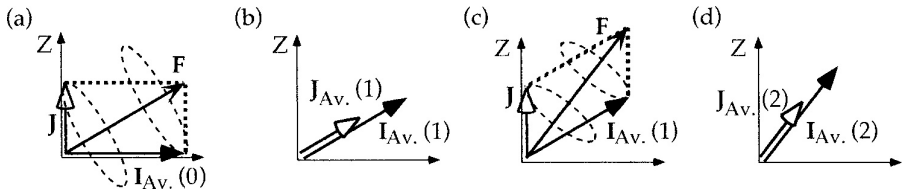

Figure 2.5: Illustration of transfer of atomic spin polarization to the nuclear spin, in a classical view. (a) With I unpolarized and J polarized, the two spins precess around the total spin direction $\mathbf{F}$. (b) On average, the observed spins are parallel to F, influenced by the polarization of J. (c-d) A successive polarization of J, for example from the multi-foil technique, increases the polarization of I further. From [17].

2.2.4 Polarization with multiple foils

In practice, many foils installed at a fixed distance are used to obtain high degrees of nuclear polarization. It can be shown that passage through N foils will provide a total transfer of $\left[G^{qq'}_{kk'}(t)\right]^N$, assuming that:

- the nuclear spin is unaffected by interactions with foils so that nuclear polarization can only be affected by the hyperfine interactions,
- only the exit surface of a foil provides atomic polarization allowing a full reset of the atomic spin polarization after a foil,
- contributions from orientations with rank > 2 are negligible based on results from experiments, and
- $\omega_{FF'}t \gg 1$, where $\omega_{FF'}$ is the quantum beat angular velocity, to allow relaxation of F for the whole spin system.

This is a key feature of the tilted foil technique, where an increased number of foils will improve the degree of polarization for the nuclear spin. With this method, it can be shown that for $I > J$, the nuclear polarization p_I can be

larger than p_J (see Figure 2.6). As described in [21] the resulting nuclear polarization can be described with a general formula:

$$p_I(N) \sim \frac{I+1}{J+1}(1-Q^N)p_J$$

where p_J is the atomic polarization which is reset after passage through each foil, N is the number of foils and Q is:

$$\begin{array}{ll} 1-\frac{2}{3}\left(\frac{J}{I}\right)^2 & \text{for} \quad I > J \\ \frac{1}{2} & \text{for} \quad I = J \\ \frac{1}{3} & \text{for} \quad I < J \end{array} \tag{2.10}$$

The polarization approaches a saturation value when F and I coincide, which should be taken into consideration with experimental issues that are related to the number of foils (energy loss and angular straggling for instance). An illustration of the increase in nuclear spin polarization by multiple foils can be seen in Figure 2.5 (c-d), and calculations based on the multi-foil theory for a selection of parameters are presented in Figure 2.6.

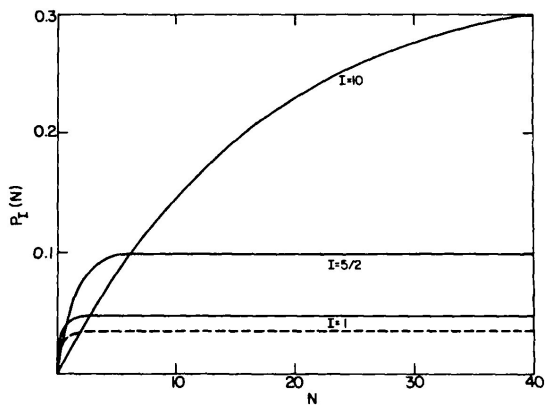

Figure 2.6: The degree of polarization in the multi-foil theory versus the number of foils and nuclear spin of the beam for $J = 5/2$ and $p_J = 0.1$ after passage through each foil. From [21].

The beam energy can play a role in the efficiency of polarization, as clearly shown in [22]. Low beam energies, in the order of 100 keV/u, are generally favored also for heavier beams (e.g. [23]).

2.3 Coulomb excitation

An important tool in nuclear structure studies is the study of level structures by observation of the gamma radiation emitted from excited states. Such states can be populated by colliding high speed projectiles with a target. In order to avoid the description of the complicated weak and strong nuclear interactions, the well understood long-range Coulomb force between the projectile and target nuclei is utilized. This type of inelastic scattering experiment is referred to as Coulomb excitation.

The safe energy is the kinetic energy of the projectile nucleus in a Coulomb excitation reaction that maximizes the reaction cross section but avoids nuclear overlapping of the participating nuclei. For the experiment presented in this thesis, the most important observations are projectile scattering distributions and the first level de-excitation gamma radiation. Using for example [24]:

$$E_{max} = 1.44\frac{A_1 + A_2}{A_2} \cdot \frac{Z_1 Z_2}{1.25(A_1^{1/3} + A_2^{1/3}) + 5} \tag{2.11}$$

designed for studies of reorientation effects, a medium heavy projectile nucleus ($Z_p \sim 10 - 20$) and a heavy target ($Z_t \sim 50 - 60$) allows for safe energies of at least 3 MeV/u.

In order to achieve a high cross section for Coulomb excitation, it may be beneficial to go beyond the safe energy. The behaviour of the outgoing products can then be characterized by, for example:

Transfer: nucleons (commonly a small amount of protons, neutrons or small bound groups of nucleons) are transferred from one nucleus to the other.

Spallation: one of the two (heavy) participating nuclei ejects nucleons.

Fragmentation: one of the two (heavy) participating nuclei splits into multiple large fragments.

Fusion: The two nuclei overlap and merge into one nucleus.

After any such reaction, the probability that the products are in their ground state is very small and further processes may take place to reduce the energy. In particular for fusion, two nuclei are merged and create a heavier nucleus exclusively in a highly excited state. The first de-excitation modes are normally very rapid expulsion of nucleons and gamma radiation. Given certain experimental settings, fusion reactions may actually be as abundant as Coulomb excitation and must be considered during preparations for experiments.

Chapter 3

^{21}Ne experimental setup

The present chapter describes the polarization experiment using stable ^{21}Ne, where the polarization degree was analyzed with the Coulomb excitation setup MINIBALL at ISOLDE.

3.1 Overview and REX beam

The experiment was designed to investigate the degree of nuclear spin polarization created with the tilted-foil method by measuring the asymmetry in the distribution of scattered particles which undergo Coulomb excitation. The major components of the experiment were REX-ISOLDE, the tilted foils device for creation of the polarization and the MINIBALL target and detectors for polarization measurement. The full setup is illustrated in Figure 3.1. In the following sections, each of the parts with settings for the experiment will be covered.

3.1.1 Beam and target

Because this experiment was designed exclusively for measuring nuclear spin polarization, ^{21}Ne was chosen as the beam so that a reliable and intense beam

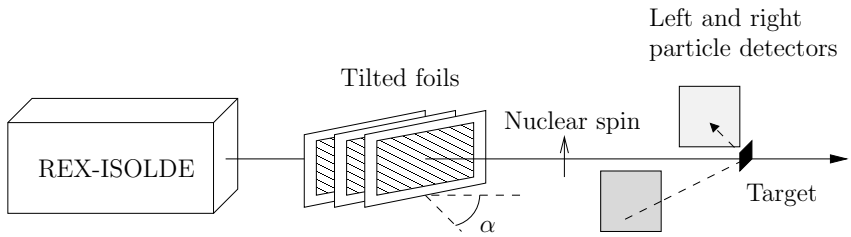

Figure 3.1: Overview of the experiment.

could be delivered. Since ^{21}Ne is a stable isotope, it was injected directly into the EBIS from a gas bottle, rather than being produced online. This provides an easily adjustable beam current in the range of 200 epA which is at least an order of magnitude higher than the nominal radioactive beam current [25]. Also, this isotope has a relatively high ground-state spin of $3/2^+$ compared to other stable and relatively light nuclei which makes it suitable to achieve high degrees of nuclear polarization (see 2.2.4). Its first few excited states are listed in Table 3.1, showing wide energy gaps between observable high-intensity transitions, which simplifies detection and analysis. The charge state selection in the REX linac was set to $q = +5$ corresponding to an $A/q = 4.2$ which separates the beam from most common contaminants from REX-EBIS, and the beam energy was set to 2.85 MeV/u to attain a high Coulomb excitaton cross sections. This is in conflict with the low energy beams normally favored for tilted foils polarization, but collected statistics were more important as Coulomb excitation cross section decreases rapidly below a few MeV/u.

At $q = +5$, the electron configuration of ^{21}Ne was $1s^2 2s^2 2p^1$ with $^2P_{1/2}$ configuration, with the atomic spin $J = 1/2$. If this was the charge state at foil exit, $I > J$ and the spin polarization of the nucleus can be expected to be larger than that of the atom.

The chosen Coulomb excitation target was ^{120}Sn, which has a first excited state at a higher energy than that of ^{21}Ne. Furthermore, it is an even-even nucleus to simplify the effect of polarization in the observed reaction channels.

Table 3.1: First excited states and intense transitions of ^{21}Ne. From [26].

E (keV)	J^π	$T_{1/2}$
0	$3/2^+$	stable
350.727(8)	$5/2^+$	7.13(14) ps
1745.911(18)	$7/2^+$	52(3) fs

ΔE (keV)	Mult.	B(E2) (W.u)
350.7	M1+E2	M1=0.0716(15), E2=24(3)
1395.1	M1+E2	M1=0.145(9), E2=11(4)

Table 3.2: First excited states and intense transitions of ^{120}Sn. From [26].

E (keV)	J^π	$T_{1/2}$
0	0^+	stable
1171.265(15)	2^+	0.640(12) ps
1875.108(25)	0^+	7.4(10) fs

ΔE (keV)	Mult.	B(E2) (W.u)
703.84(2)	E2	E2=12.6(17)
1171.25(2)	E2	E2=11.41(22)

The first few excited states of ^{120}Sn are listed in Table 3.2. It may be worth mentioning that a negligible number of detected gammas were emitted due to de-excitations in the target compared to that of the projectiles. Therefore, all observed Coulomb excitation reactions can be assumed to leave the target nuclei in the 0^+ ground state.

3.2 Foils and tilting holder

To reduce the effects of the tilted foils on the beam, the foils were kept as thin as possible. For this experiment, self-supporting pure carbon foils with the density 4 µg/cm^2 and a surface area of approximately 5 cm^2 were used.

The setup to hold the thin tilted foils was designed and manufactured as a general purpose device and was easily integrated into the beam-line approx-

imately 1 m upstream of the Coulomb excitation setup [27], see Figure 3.2. A stepper motor allowed to remotely control the tilting angle of the foils during the experiment. Changing the tilt angle allows to reduce systematic errors in detection efficiency. If the beam interacts with the foil holder, the different geometries may introduce further systematic errors.

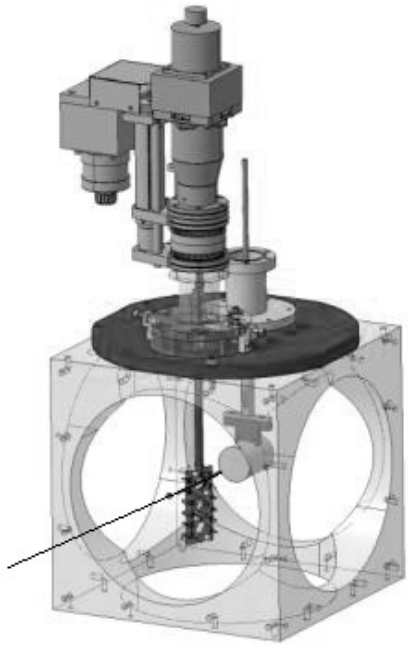

Figure 3.2: Schematic view of the foil holder and tilting mechanism, installed 1 m upstream of the target chamber in the MINIBALL experimental setup. The line entering the diagnostics box represents the beam passing through the foils. From [27].

The holder was designed with three windows in order to allow switching between three foil configurations without the need to break the beamline vacuum. This may be useful to monitor potential scattering on frames without foils and to shoot the beam through different numbers of foils. For this experiment, an empty frame was installed in the top window for reference

measurements, one foil in the middle window and three foils in the bottom window. Figure 3.3 shows the loaded foil holder prior to the experimental run. The distance between the three foils in the bottom window was 1 mm, which with a tilting angle of 70° corresponds to almost 3 mm effective spacing for the traveling beam.

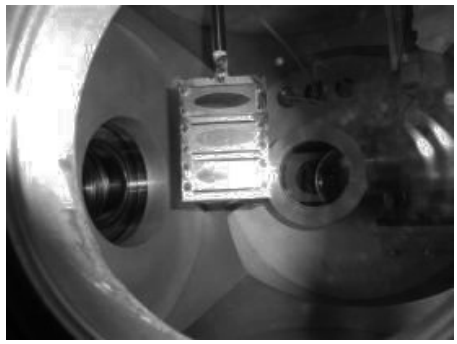

Figure 3.3: Foil holder loaded with foils for the experiment. The top window contains an empty frame for beam diagnostics purposes, the middle window one foil and the bottom window three foils. From [27].

The programming interface consisted of a custom high level scripting language designed specifically for the stepper driver. It was versatile enough to allow fine tuning of motor speeds to reduce mechanical vibrations that may put mechanical stresses on the fragile foils. To further reduce the vibrations, the stepper driver was modified for a reduction in supplied motor current. The actual program can be found in [27] and it performed the following routine:

- Orient foils at $-70°$ and wait for 3 minutes.
- Orient foils perpendicular to the beam and wait for 30 seconds.
- Orient foils at $+70°$ and wait for 3 minutes.

3.3 MINIBALL

MINIBALL [28], schematically depicted in Figure 3.4, is a gamma spectrometer located behind REX-ISOLDE which was used int the Coulomb excitation measurement. Due to the estimated low beam intensities and therefore small number of reactions of interest for radioactive beams from ISOLDE, high detection efficiency was emphasized when making the device. High angular precision was also important, not only to attain good peak-to-noise ratios but also for particle correlation to remove artifacts such as gamma frequency Doppler shift.

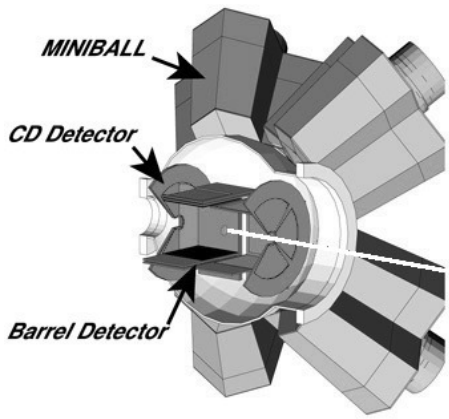

Figure 3.4: MINIBALL HPGe detectors with the barrel shaped T-REX particle detector setup installed around the target. The white line represents the beam impinging on the target in the middle of T-REX. From [29].

There are eight triplet clusters of HPGe crystals in the MINIBALL setup, where every triplet is cooled by cold fingers to liquid nitrogen temperature. Every crystal is segmented into six symmetric parts, making for a total of $8 \times 3 \times 6 = 144$ active segments yielding excellent angular resolution. The clusters are mounted on a flexible armature with three rotational degrees of freedom (not considering near Gimbal lock at extreme angles) which allows the detectors to be positioned very close to the target chamber, down to 12 cm

from the target. When all clusters are installed, the solid-angle coverage is approximately 60% of the full 4π. The intrinsic energy resolution of the crystals is 2.3 keV at $E_\gamma = 1.3$ MeV.

With the digital XIA Digital Gamma Finder (DGF) 4 channel data acquisition modules [30] at MINIBALL, it is possible to acquire digitized samplings of signals from the HPGe detectors. This level of granularity can be used for pulse shape analysis (PSA). By analyzing the shapes of the signals of one event, the impact point inside a crystal can be determined with an angular precision higher than the crystal segmentation. The two major disadvantages to this additional precision are that every gamma event will allocate much more storage space (a sampled signal rather than a single energy value) and the complexity of the analysis increases manyfold. Previous tests with PSA at MINIBALL have shown that the increased precision has not provided significantly better Doppler correction so the full sampled HPGe signal shapes are normally not taken into account [31].

3.3.1 Particle detection with the MINIBALL T-REX chamber

The detection of recoil ions after Coulomb excitation is carried out with silicon detectors inside the target chamber. One of the detectors is constructed from concentric arcs of silicon and is called the CD detector, for reasons clear by Figure 3.7a. Depending on the experiment, elastic scattering may have significantly higher cross sections than Coulomb excitation in the forward scattering angles. This is especially true for light beams on heavy targets, in which case the CD detector is mounted upstreams of the target for detection of backwards scattered particles. Pictorially, at these angles, beam ions have undergone collisions with small impact parameters which increases the Coulomb potential and the likelihood of Coulomb excitation, whereas large impact parameters lead to forward scattering.

In transfer experiments performed in inverse kinematics with a heavy ion impinging on a light target, the typical maximum in cross-section for small

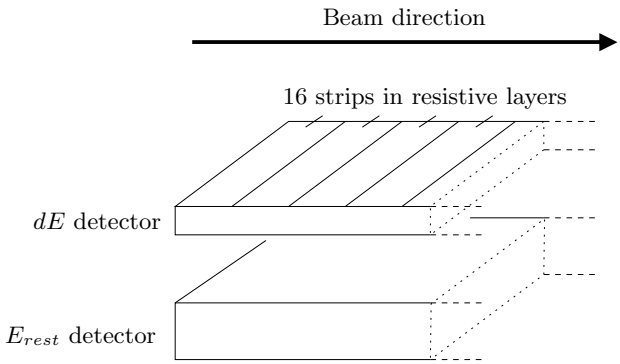

Figure 3.5: Schematic of the side layers in the T-REX barrel detector. The dE and the E_{rest} layers are 150 µm and 1000 µm thick, respectively.

angles in the centre-of-mass system will translate in a large distribution of scattering angles in the laboratory system. For this purpose, the T-REX detector setup [29] was constructed for detecting mainly very light charged particles, such as protons, deuterons, tritons and α-particles. Each detector consists of two silicon detectors, pictured in Figure 3.5. One side of the first detector, which is approximately 150 µm thick, has a resistive layer segmented perpendicularly to the beam direction into 16 strips for reliable determination of the deviation angle θ from a reaction. The backside of this detector is read out with one signal and can together with the stripped readouts be used to reconstruct the impact point along a strip. The second layer is 1000 µm thick and will stop most particles, thus measuring their residual energy. Together, the two layers can be used to determine the angular coordinates of the charged particles and the kinematical curves. The layout of the detectors in the T-REX barrel-shape setup can be seen in Figure 3.6 and Figure 3.7b.

The problem of elastic scattering of the beam previously discussed still applies for the T-REX silicon detectors. This is especially true for high intensity stable beams, like in this project. To resolve this issue, the detectors in the forward scattering angles were protected with a 12 µm-thick Mylar foil.

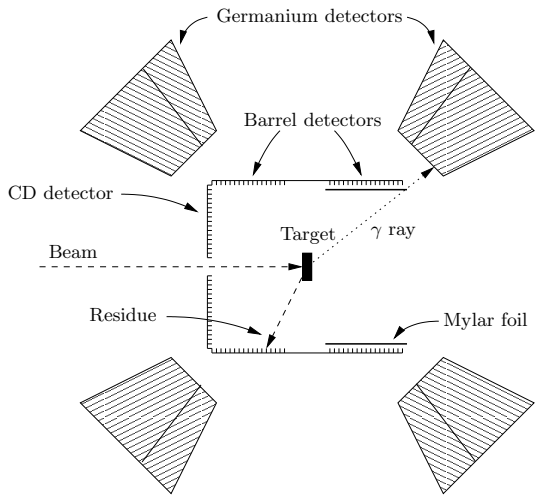

Figure 3.6: Schematic of the MINIBALL and T-REX setup detector configuration used for the experiment.

3.3.2 Electronics and data acquisition

Energy signals from the HPGe gamma detectors were sampled and time-stamped with XIA DGF 4C modules. Barrel particle detector signals were collected with MADC32 ADC modules which implement timestamping. The CD-detector signals were collected with CAEN 785 ADC modules, which due to a lack of timestamping capability were timed with a DGF with the CD-detector trigger signal. All trigger signals were collected and subject to OR gates at which point all modules were queried by the data acquisition. Data acquisition was controlled via the MARaBOU [32] system based on MBS [33], which supports online analysis of the collected raw data. For a more detailed explanation of the MINIBALL data acquisition system, see [34].

3.3.3 MINIBALL setting up

The ^{21}Ne beam was impinging on the self supporting ^{60}Ni and ^{120}Sn target foils with densities 2.0 mg/cm^2 and 2.06 mg/cm^2, respectively. Due to the

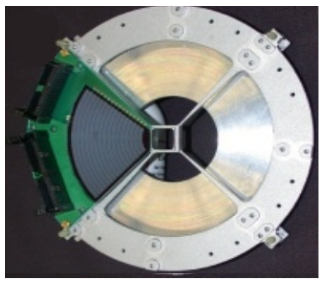

(a) Photo of the annular CD detector. From [28].

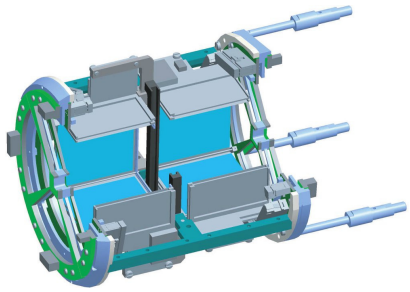

(b) Schematic of the T-REX chamber. Normally, only one CD detector is mounted at one end of the barrel structure. From [35].

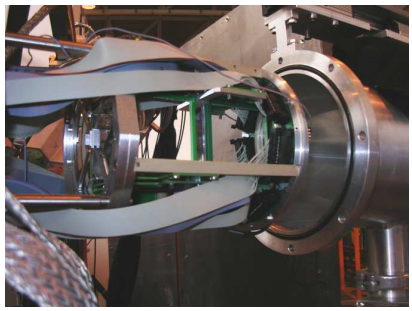

(c) The T-REX chamber installed at the target location. From [36].

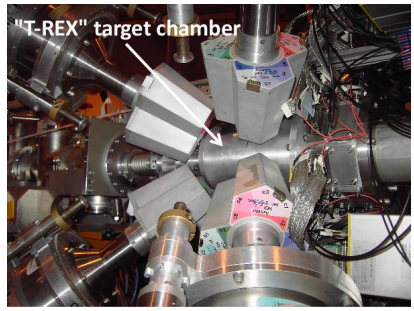

(d) Target chamber closed and surrounded by the HPGe detectors. From [28].

Figure 3.7: Detailed views of the T-REX particle detector setup and mounting inside MINIBALL.

Table 3.3: Signals transmitted by the stepper driver to the MINIBALL data acquisition for foil orientation status in the event data. The bitmask is a decimal representation of the two binary signals for analysis.

Tilting angle	Turning	$-70°$	$0°$	$+70°$
Signal 1	0	1	0	1
Signal 2	0	0	1	1
Bitmask	0	1	2	3

low nuclear excitation energies of ^{60}Ni, a large number of background events were recorded, which prompted an early switch to the heavier ^{120}Sn target. A deuterated polyethylene foil was installed at the target position during the experiment for calibration purposes which will be treated in detail in the data analysis chapter.

The experiment prior to the present one utilized a setup suitable to our needs, including the T-REX setup with Mylar protection against abundant elastic scattering. In the early phases of the experiment, the elastic scattering in the forward T-REX detectors showed very high trigger rates that introduced dead time for the full acquisition system. These trigger signals were removed and the system then triggered only on gamma events and backwards scattered particles. Two signals from the stepper driver were connected to an ADC so that the orientation status of the foils was available in the event data stream, see Table 3.3.

Chapter 4

Experimental results and discussion

4.1 Calculations and kinematics

Ion beams with energies of a few MeV/u reach almost 10% of the speed of light, which introduces noticeable relativistic effects that need to be taken into account. LISE++ [37] was used to calculate kinematics curves in lab angles, for example $E_{(^{21}\mathrm{Ne})}(\theta_{(^{21}\mathrm{Ne})})$ after collision with ^{120}Sn which is shown in Figure 4.1. This curve is useful for filtering the highly energetic neon ions from other detected particles which would have different kinematics curves.

4.1.1 Coulomb excitation cross sections

The Fortran program *CLX* [38], provided by the MINIBALL collaboration, was used to calculate the cross section $d\sigma/d\theta$ for Coulomb excitation of specific nuclear energy levels. The input parameters include beam and target properties, nuclear levels and transitions of interest and annular particle detector geometry. Calculations for the first excited level of ^{21}Ne with the T-REX and CD detectors are presented in Figure 4.2 with data from Table 4.1 and

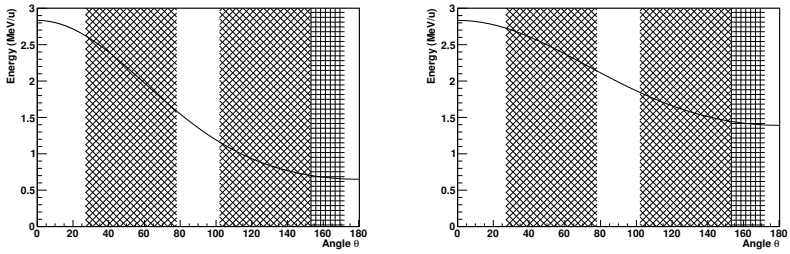

(a) ^{60}Ni (b) ^{120}Sn

Figure 4.1: Kinematical curves for ^{21}Ne colliding with ^{60}Ni and ^{120}Sn. The diagonal cross hatches represent the coverage in the angle θ by the T-REX barrel detectors and the straight hatches represent the CD detector.

4.2. The values for the backward CD rings are correct because of the simple geometrical relationship between annular rings and scattering angles, but the values for the barrel strips are not. In space, a constant polar angle forms a cone for all azimuthal angles around the beam direction and the projection of such a cone on a flat detector surface is a curved line spanning several strips. However, since the cross section data were to be used solely for the comparison of the T-REX particle detectors, the polar angle for the silicon detectors was chosen to refer to the middle of barrel strips. According to the trend of the cross sections, the total cross section for a strip is slightly overestimated for the backward barrel strips and vice versa for the forward barrel strips. The results show differences between the barrel detectors and the backward CD by some orders of magnitude. Therefore, since the backward CD contributed little in terms of statistics and that the three layers of silicon require complicated analysis, it was not used in the final analysis.

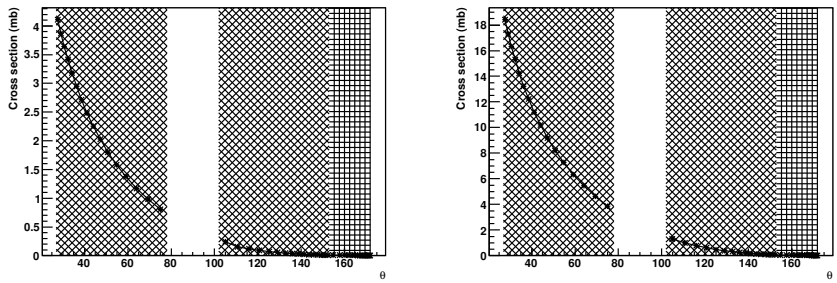

Figure 4.2: Coulomb excitation cross sections for the first excited state of ^{21}Ne impinging on ^{60}Ni (left) and ^{120}Sn (right), leading to 351 keV gamma decay. Banded regions explained for Figure 4.1. Data taken from Table 4.1 and 4.2.

	Forward		Backward	
Strip	^{60}Ni	^{120}Sn	^{60}Ni	^{120}Sn
0	0.8070	3.8544	0.2465	1.2913
1	0.9821	4.6234	0.1557	1.0089
2	1.1705	5.4532	0.1195	0.7882
3	1.3730	6.3329	0.0922	0.6175
4	1.5845	7.2666	0.0716	0.4860
5	1.8024	8.2139	0.0559	0.3855
6	2.0279	9.1857	0.0443	0.3082
7	2.2547	10.1944	0.0355	0.2475
8	2.4819	11.1747	0.0286	0.2028
9	2.7122	12.2267	0.0234	0.1666
10	2.9479	13.2176	0.0191	0.1371
11	3.1783	14.2238	0.0160	0.1151
12	3.4176	15.2996	0.0134	0.0972
13	3.6406	16.3151	0.0114	0.0821
14	3.8708	17.3039	0.0097	0.0699
15	4.1093	18.4233	0.0082	0.0607

Table 4.1: Cross sections in mb for ^{21}Ne Coulomb excited to the first excited state hitting the middle of the strips in the barrel detectors. Note that the values are over- and underestimated for the backward and forward detectors respectively, due to the curvature of constant polar angle from the scattering reaction. Strip 0 is closest to the target, strip 15 is the furthest away.

Ring	^{60}Ni	^{120}Sn
0	0.0077	0.0468
1	0.0074	0.0455
2	0.0073	0.0438
3	0.0070	0.0429
4	0.0066	0.0405
5	0.0063	0.0389
6	0.0061	0.0371
7	0.0056	0.0346
8	0.0053	0.0328
9	0.0049	0.0308
10	0.0046	0.0279
11	0.0042	0.0258
12	0.0037	0.0235
13	0.0033	0.0208
14	0.0029	0.0182
15	0.0025	0.0155

Table 4.2: Cross sections in mb for ^{21}Ne Coulomb excited to the first excited state hitting the backward CD rings. Strip 0 is for the outermost annular ring, strip 15 is for the innermost close to the beam.

Table 4.3: Fusion evaporation cross sections for ^{21}Ne on ^{60}Ni and on ^{120}Sn, calculated with PACE4 in LISE++ [37]. Products with small cross sections have been omitted from this table, so the sum is smaller than 100%. The zero cross section for ^{120}Sn means cross sections smaller than 10^{-20} mb as reported by PACE4. This is not surprising because the beam energy is very close to the safe energy, see text.

Nucleus	Proportion	Cross section (mb)
^{78}Kr	34.8%	132
^{78}Rb	20.2%	76.8
^{75}Br	11.6%	44.2
^{79}Rb	6.40%	24.4
^{76}Kr	6.29%	23.9
^{138}Nd	75.2%	0
^{139}Nd	10.9%	0
^{138}Pr	9.06%	0
^{139}Pr	2.66%	0
^{135}Ce	1.07%	0

4.1.2 Fusion evaporation cross sections

Fusion evaporation cross sections of ^{21}Ne + ^{60}Ni and ^{21}Ne + ^{120}Sn reactions are given in table 4.3. ^{120}Sn was the optimal target for the experiment, although ^{60}Ni was tested as well for comparison. The data confirms that fusion evaporation should yield events of almost the same amount of statistics as Coulomb excitation in the gamma spectra with ^{60}Ni, but not with ^{120}Sn. According to Equation 2.11, the integrated safe energy for ^{60}Ni is 1.94 MeV and for ^{120}Sn 2.76 MeV, with the latter being very close to the full beam energy.

4.1.3 Energy losses

Due to the 7.12 ps half life of the first excited state of ^{21}Ne, the de-excitation may occur anywhere inside or very close to the target. The excited nuclei therefore have kinetic energies below the beam energy of 2.85 MeV/u. The full energy range goes from 2.845 MeV/u due to losses in the tilted carbon foils down to 0.72 MeV/u when an ion is subjected to Coulomb excitation at

the end of the target and thus traverses the target twice before being detected in the backward hemisphere of the setup. This uncertainty in energy for the residue particles will broaden the kinematics curves significantly and may make this type of particle identification difficult.

4.2 Detector calibration

4.2.1 Doppler correction

The beam energies used in the experiment cause relativistic Doppler shift broadening of de-excitation gamma radiation peaks. Since $E = h\nu$ for photons, the correct gamma energy E_0 in the emitter frame can be easily calculated with:

$$E_0 \quad = \quad E\gamma(1 - \beta\cos\theta) \tag{4.1}$$

where E is the observed gamma energy, γ and β are the relativistic parameters of the emitter and θ is the angle between the momentum vector of the emitting nucleus and the observing direction. γ and β are estimated from the beam energy and the angle θ was determined from recorded angular detector coordinates.

This relatively simple expression is not only used to Doppler-correct gamma spectra, but can help calibrating the experimental setup. By fixing the beam energy which relates to β and γ and using a reaction with well known kinematics curves, it is possible to extract θ from Equation 4.1 and solve for the θ angles of the gamma detectors. This will be treated in more detail later.

4.2.2 Energy and position calibration

Calibration parameters for online analysis were kept from the experiment preceding the ^{21}Ne experiment. The gamma detectors had been calibrated with stationary radioactive sources ^{152}Eu and ^{60}Co, and the particle detectors with a mixed α source consisting of the four isotopes ^{148}Gd, ^{239}Pu, ^{241}Am and

^{244}Cm with the α-energies 3.18 MeV, 5.16 MeV, 5.49 MeV and 5.81 MeV, respectively. Least squares linear fits were performed for every detector to obtain linear calibration curves, and fitting with higher order terms was tested but did not improve the calibration and was left out. To increase the calibration statistics, the experimental data was also used during the offline analysis.

HPGe gamma detectors

As was briefly mentioned in Section 4.2.1 on Doppler correction, it is possible to estimate the angle θ of gamma detectors given data from a reaction with well known kinematics. At MINIBALL, the ^{22}Ne(d,p)^{23}Ne transfer reaction, with stable ^{22}Ne ions impinging on a deuterated polyethylene target, is regularly used to calibrate the exact position of the gamma detectors. This approach gives higher angular precision than reading coordinates from the detectors armature and circumvents mechanical errors. The deviation of the beam ejectile is in the order of 5° which can be approximated by zero deviation, and Doppler broadening is very small because of the small energy losses in the light target. The reaction ^{21}Ne(d,p)^{22}Ne was used instead of the ^{22}Ne(d,p)^{23}Ne reaction, because they have similar characteristics and let the beam setup remain unchanged for this experiment.

Due to the rigid geometric relationship between segments in a full cluster, given rough estimates and taking into account possible geometrical reflection and symmetries, all three angular coordinates can be extracted. The three angular coordinates of a cluster were adjusted iteratively by a custom written program and the Doppler correction for a set of coordinates was used to evaluate a fitness value to find an optimal set of angular coordinates.

In principle, it is possible to reconstruct the small residue angle of the outgoing ^{22}Ne by observing the proton. The deviation angles of the ejectile and residue are determinate, and the relationship is shown in Figure 4.3 as calculated by LISE++. Using this kinematics curve $\theta_{(^{22}Ne)}(\theta_p)$, the angle θ in Equation 4.1 between the ^{22}Ne and the gamma rays can be calculated exactly. The correction is very small in this calibration run, but may be of

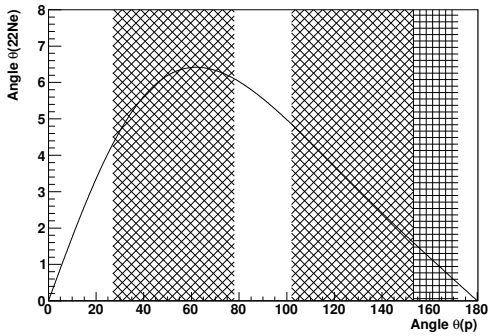

Figure 4.3: Kinematical curve between θ_p and $\theta_{^{22}Ne}$ for ^{21}Ne(d,p)^{22}Ne reaction. Banded regions are explained in Figure 4.2.

use in experiments which demand very accurate Doppler correction for larger residue deviation angles. Most counting experiments can be designed such that the resolving of gamma peaks is not necessary, as is the case with this polarization measurement experiment. Other approximations in the analysis, such as point-like detectors and simplifications of energy losses in the target, may contribute with further Doppler broadening.

Results from the Doppler correction of the ^{21}Ne(d,p)^{22}Ne calibration runs are presented in Figure 4.4.

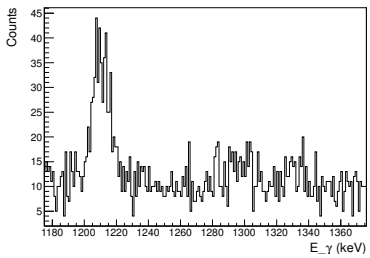

(a) Not Doppler corrected $(0, A, 0)$.

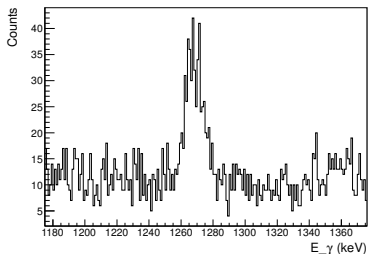

(b) Doppler corrected $(0, A, 0)$.

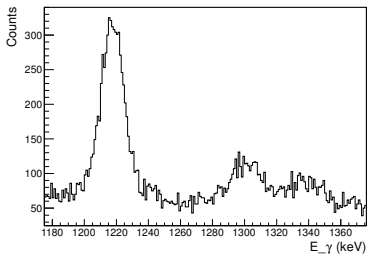

(c) Not Doppler corrected $(0, A, core)$.

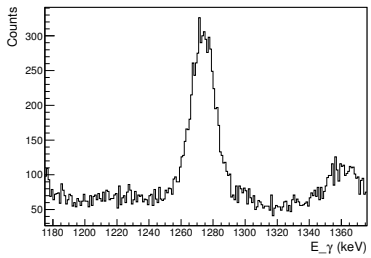

(d) Doppler corrected $(0, A, core)$.

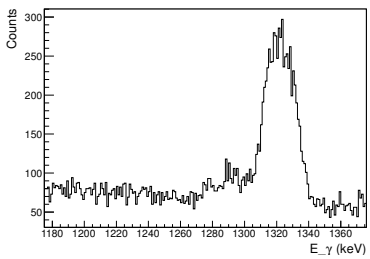

(e) Not Doppler corrected $(1, A, core)$.

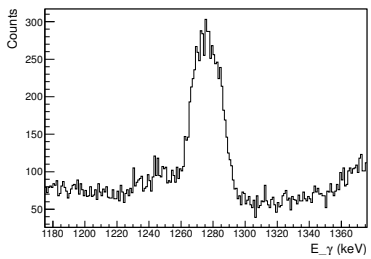

(f) Doppler corrected $(1, A, core)$.

Figure 4.4: Position-calibrated and Doppler-corrected gamma spectra of a germanium segment and two cores from the ^{21}Ne(d,p)^{22}Ne reaction runs. The parentheses notation means (cluster $\in \{0..7\}$, crystal $\in \{A, B, C\}$, segment $\in \{core, 0..5\}$). Note that clusters 0 and 1 detected gamma radiation in the backwards and forwards angles, respectively. The peaks can be narrowed further if the small deviation angle of the residue ^{22}Ne is reconstructed, but these spectra are used for angular coordinate calibration of the HPGe detecters, not the energy values.

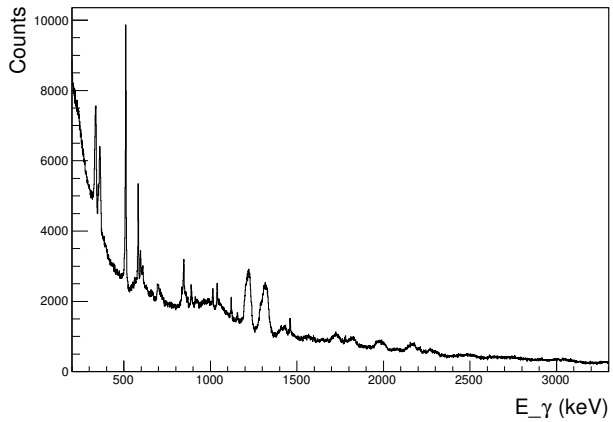

(a) Not Doppler corrected.

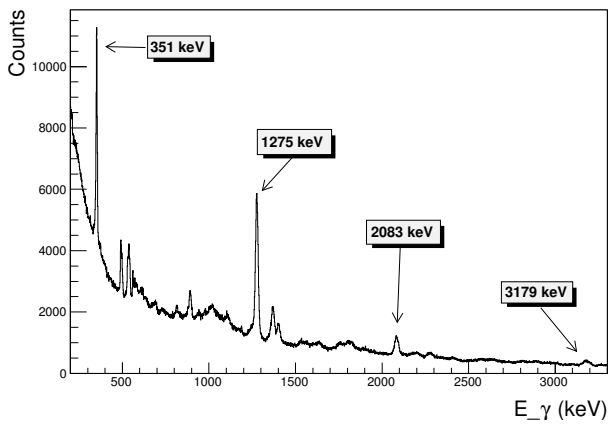

(b) Doppler corrected.

Figure 4.5: Energy calibrated gamma spectra from the ^{21}Ne(d,p)^{22}Ne reaction runs. Energies taken from the germanium cores and angular position from the segments. Notice that by optimizing Doppler correction for the first excited state in ^{22}Ne at 1274 keV, three other peaks are corrected; the first excited state of ^{21}Ne at 351 keV and the second and third excited states of ^{22}Ne at 2083 keV and 3179 keV. High gamma energies were not calibrated which may cause the broad high energy peaks. The sharp positron electron annihilation line at 511 keV is of course destroyed by the Doppler correction.

Position information along the strips in the silicon detectors can be obtained with:

$$x = C\frac{E_{\text{resistive}}}{dE}$$

where x is the position ($x = 1$ is at the readout end and $x = 0$ is at the other end of the strip), $E_{\text{resistive}}$ is the readout from the resistive layer for the strip in question, dE is the readout on the rear side of the same silicon detector slab and C is a calibration coefficient. An example from a calibration run can be seen in Figure 4.6.

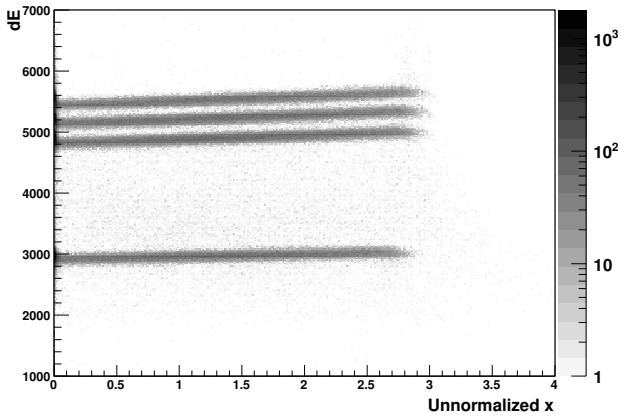

Figure 4.6: Partial position calibration with a mixed alpha source (refer to the energy calibration section for more information). The full calibration to resolve the position dependence on the energy was not carried out due to problems in the data which will be covered in the discussion section.

4.3 Event selection

The prompt peak gating between gamma and particle observations was set to:

$$|t_p - t_\gamma + t_{of}| < 100\,\text{ns}$$

where t_p and t_γ are the time stamps for a particle and a gamma ray respectively, and $t_{of} = 150\,\text{ns}$ is a correction term due to a non zero time-stamp offset between the modules for gamma and particle detectors. The prompt gate was verified for both targets ^{60}Ni and ^{120}Sn.

The gating condition on the detected gamma rays for the excited ^{21}Ne consists of keeping events with a gamma line at 350.7 keV. The effective width of the Doppler-corrected 350.7 keV gamma line was determined to be 20 keV.

Kinematical particle selection using the curve in Figure 4.1 was difficult to perform due to energy losses in the target as has been suggested. The results section will verify this. Instead, because the ^{21}Ne with an energy up to 2.85 MeV/u was the most energetic particles in the reactions, a lower threshold at 6 MeV was introduced to remove random coincidences. The value was found by increasing the threshold from zero until the integral of the 350.7 keV gamma line over the signal baseline started decreasing.

4.3.1 Polarization signature

As shown in the section on formal polarization in the theory chapter, the nuclear spin polarization can be related to the scattering asymmetry perpendicular to the polarization and beam axis as in Equation 2.9. A slight rearrangement of that expression yields:

$$A = \frac{L-R}{L+R} = \frac{1-R/L}{1+R/L} = \frac{1-\rho}{1+\rho}, \quad \rho = R/L \tag{4.2}$$

where the counting rates L and R were taken as the integrals of detected particles in the T-REX detectors in the backwards directions on either side of the target. It is possible to cancel the left and right detection efficiencies ε_R and ε_L by making use of a double ratio geometric mean. The difference between tilting the polarizing foils at $\alpha = -70^\circ$ and $\alpha = +70^\circ$ is that the polarization direction will switch sign, but the magnitude will not change. Seen from another perspective, the left and right detectors have been switched. Thus the ratio R/L can be measured in two equivalent ways: $R(\alpha = -70^\circ)/L(\alpha = -70^\circ)$ and $L(\alpha = +70^\circ)/R(\alpha = +70^\circ)$. By taking the geometric mean of the two ratios, the efficiencies from the two detectors cancel out and the final asymmetry expression is thus:

$$A' = \frac{1-\rho'}{1+\rho'}, \quad \rho' = \sqrt{\frac{R(+\alpha)L(-\alpha)}{L(+\alpha)R(-\alpha)}}, \quad \alpha > 0 \tag{4.3}$$

Note that tilting the foil holder changes the geometrical configuration of the experimental setup. If the beam is not aligned perfectly with the experimental setup, unknown systematic errors may be introduced with this double ratio method.

By tilting the foils perpendicularly to the beam direction, in which case no polarization is expected (however alignment may be induced along the beam direction [20]), any observed asymmetry would be a baseline asymmetry for other measurements. The double ratio method cannot be applied in this case, but Equation 2.9 can be used directly instead. All asymmetry measurements need to be evaluated with this equation to make any comparisons valid. Nevertheless, it is possible to combine a perpendicular foil measurement with an oblique foil angle measurement in a double ratio with:

$$\rho'_{+\alpha,0} = \sqrt{\frac{R(+\alpha)L(0)}{L(+\alpha)R(0)}} \tag{4.4}$$

$$\rho'_{-\alpha,0} = \sqrt{\frac{R(-\alpha)L(0)}{L(-\alpha)R(0)}} \tag{4.5}$$

4.4 Gamma and particle spectra

In total, after event selection, a little more than 1200 events had been collected. Energy calibrated gamma spectra without Doppler correction for both ^{60}Ni and ^{120}Sn targets are shown in Figure 4.7.

Due to protective foils and large amounts of elastically scattered ^{21}Ne, data from the detectors in the forward part of T-REX will not be presented. The ejectiles did not pass through the dE detectors in the backwards angles, so the thick E_{rest} detectors in the backwards angles will be absent. This prevents E vs dE plots for unambiguous particle identification. Finally, the reaction cross section in the angles covered by the CD detector are orders of magnitudes smaller than in the angles covered by the T-REX detectors, so final analysis was not performed using this detector.

Cross-talk histograms between the strips of the resistive layer in the dE detectors are presented in Figure 4.8, showing no discernible cross talk between adjacent strips. Thus, the polar angle from strip identification should be reliable. Figure 4.9 shows the correlation plot of dE against $E_{\text{resistive}}$ which shows saturation issues for high energy particles. This hindered length-wise strip coordinate reconstruction which would have increased the precision in kinematics calculations. Particularly Doppler correction and $dE(\theta)$ particle filtering suffered from this issue.

Correlations between dE and deviation angle with a gate around the first excited state in ^{21}Ne is shown in Figure 4.10. Structures resembling the kinematical curves in 4.1 were expected but not present. Random coincidence events were cut with a low energy threshold of 6 MeV as described before.

The first excited state of ^{21}Ne with Doppler correction based on the information from calibrated particle spectra is presented in Figure 4.11.

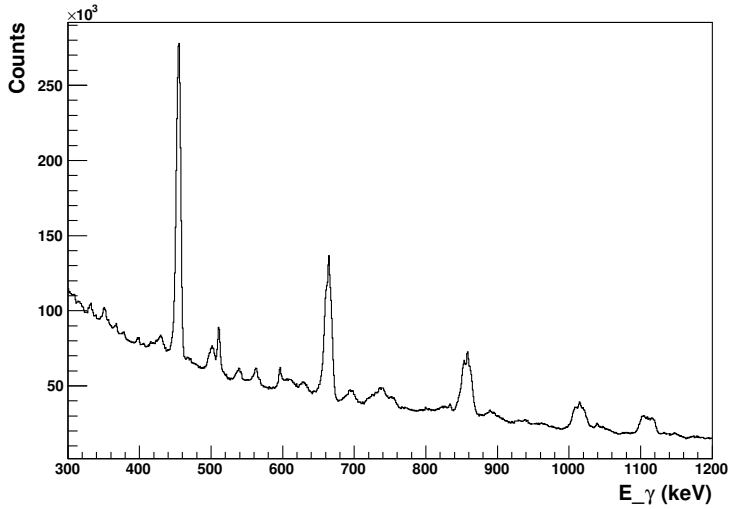

(a) ^{60}Ni target.

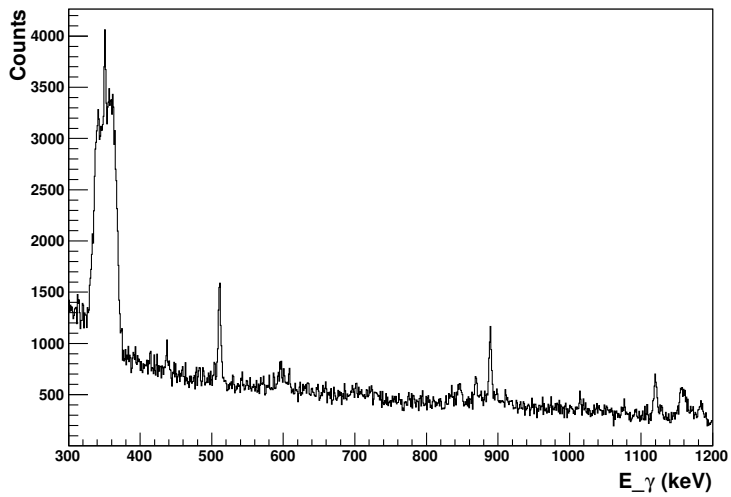

(b) ^{120}Sn target.

Figure 4.7: Energy calibrated gamma spectra from all runs with ^{21}Ne on (a) ^{60}Ni and (b) ^{120}Sn. Note that the first excited state in ^{21}Ne at 351 keV vanished among the very high background noise with the ^{60}Ni target.

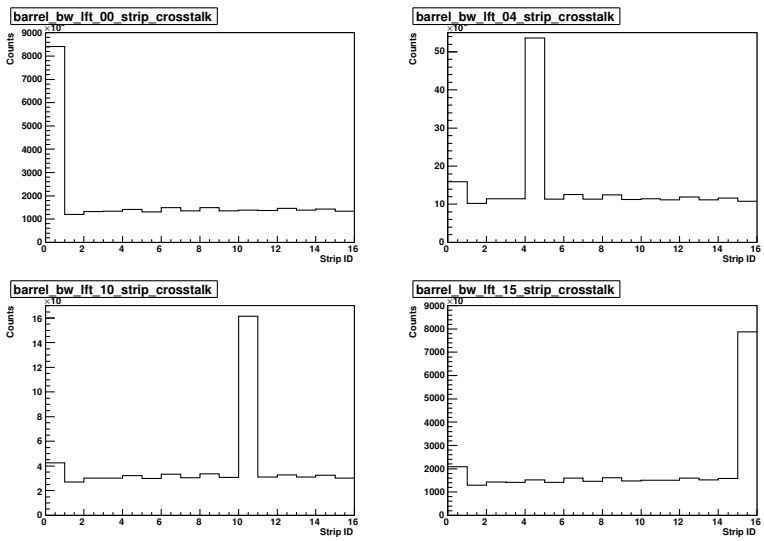

Figure 4.8: Accumulated readouts from strips in the backward-left dE detector for events where one of strip 0, 4, 10 and 15 (0 closest to the target) was found to have the strongest signal. Cross talk would have been characterized by slopes on either side of the selected strips. The additional statistics in the first strip can be seen in all cross-talk histograms.

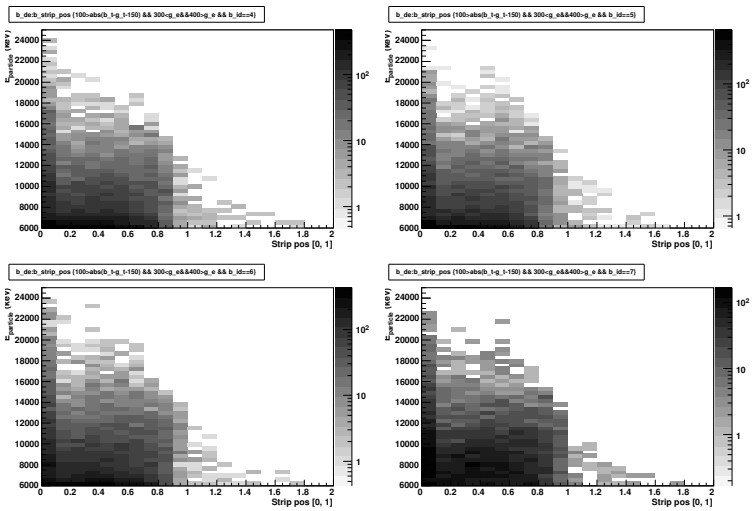

(a) ^{60}Ni target.

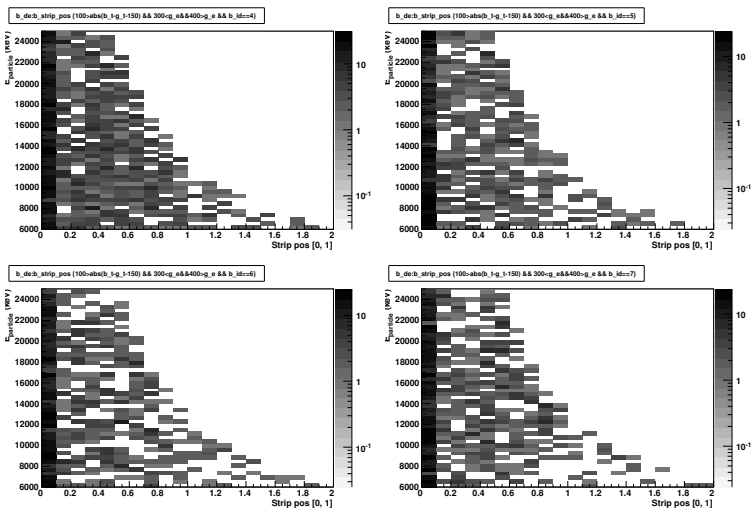

(b) ^{120}Sn target.

Figure 4.9: dE vs resistive layer plots to reconstruct length-wise strip position according to Equation 4.2. Readout saturation issues can be seen at high energies. The higher recoil energy with the ^{120}Sn target makes reconstruction particularly difficult.

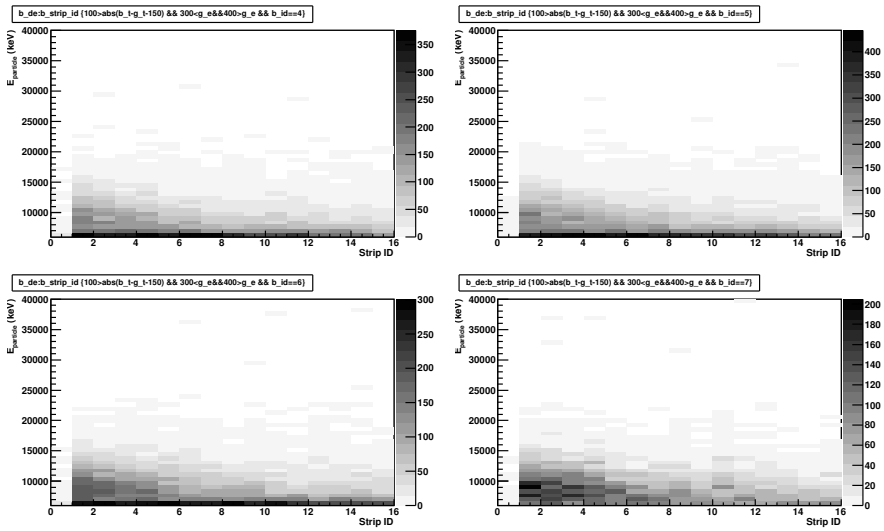

(a) ^{60}Ni target.

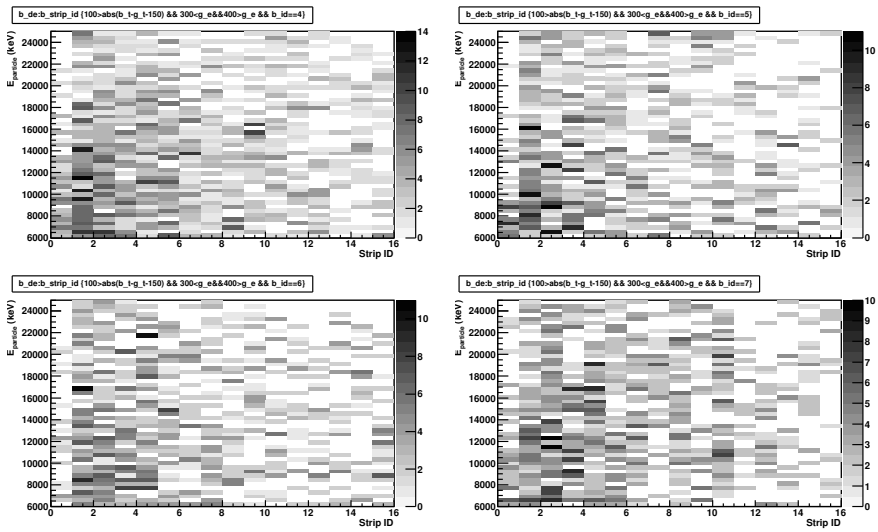

(b) ^{120}Sn target.

Figure 4.10: Backward barrel dE vs strip id with a gamma gate around the first excited state at 351 keV in ^{21}Ne. Particles below 6 MeV consist of random coincidences which was investigated with gamma peak integrals. Compare to the kinematics curves in Figure 4.1 (note the difference in units).

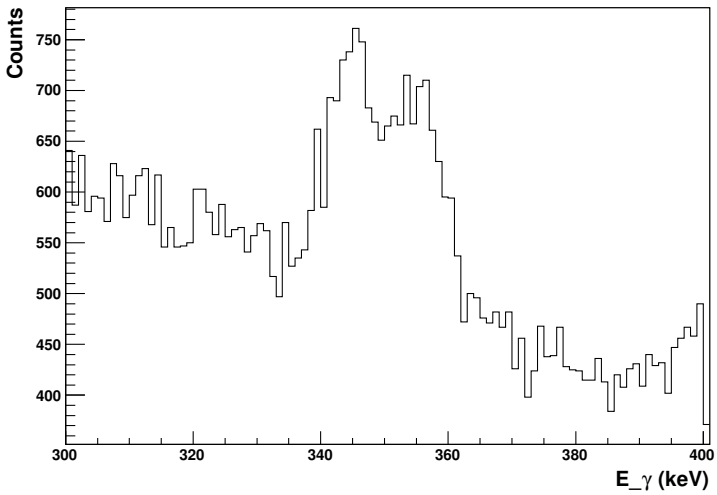

(a) ^{60}Ni target.

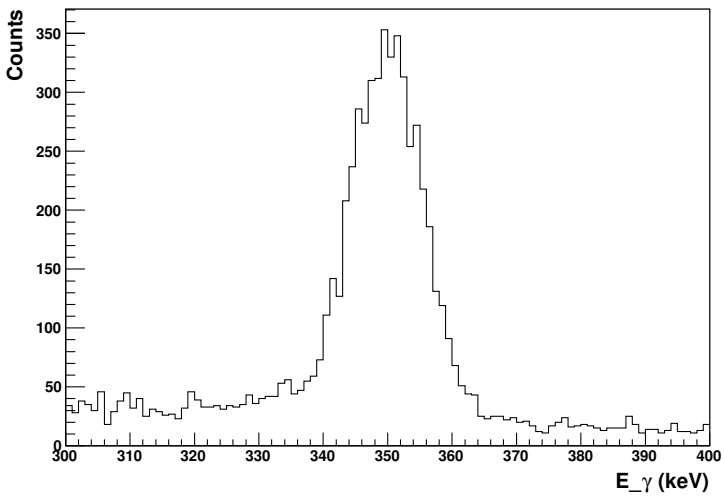

(b) ^{120}Sn target.

Figure 4.11: Doppler-corrected first excited state of ^{21}Ne. Notice the small signal-to-noise ratio with the ^{60}Ni target compared to ^{120}Sn.

4.5 Asymmetry value

Raw particle counts used in the calculations are given in Table 4.4 and 4.5.

Table 4.4: Raw integrated event counts after event selection.

Detector	$\alpha = -70°$	$\alpha = +70°$	$\alpha = 0°$
Left	854	764	153
Up	562	598	101
Right	540	517	96
Down	572	486	82

Table 4.5: Raw counting rates separated into ten batches. For $\alpha = 0°$, the data were divided into five batches due to low statistics by combining two batches from the oblique angle calculations.

Batch #	L/R $\alpha = -70°$	L/R $\alpha = +70°$	L/R $\alpha = 0°$
0	85/71	44/60	18/19
1	83/23	64/40	-
2	67/55	77/40	18/23
3	76/58	81/69	-
4	89/61	75/53	35/20
5	97/41	83/37	-
6	95/53	82/38	40/27
7	91/79	90/55	-
8	84/66	97/71	42/7
9	87/33	71/54	-
Batch #	U/D $\alpha = -70°$	U/D $\alpha = +70°$	U/D $\alpha = 0°$
0	15/81	14/51	16/11
1	47/50	48/26	-
2	74/44	70/48	22/21
3	57/66	59/70	-
4	42/18	48/27	14/3
5	75/18	81/15	-
6	65/59	93/47	24/24
7	70/78	75/63	-
8	66/78	68/82	25/23
9	51/80	42/57	-

The double ratio asymmetry, from Equation 4.3, and statistical error of integrated event counts in the particle detectors are presented in Figure 4.12 with exact values in Table 4.6. Errors will be assumed to originate purely from Poission counting statistics. Six double ratio asymmetries were calculated, combining runs with $\alpha = \{-70°, +70°, 0°\}$ and left-right or up-down detector pairs. Raw event counts can be found in Table 4.4.

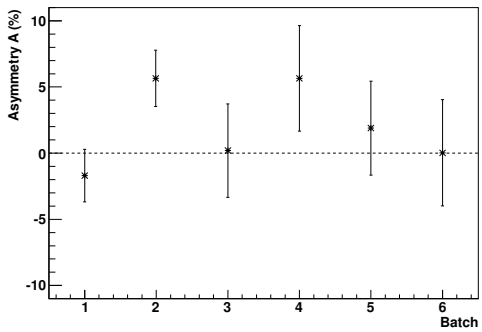

Figure 4.12: Double ratio asymmetries calculated from combinations of detector pairs and foil angles. Exact values and the asymmetry configurations on the horizontal axis can be found in Table 4.6.

Table 4.6: Double ratio asymmetries with permuted combinations of ratios and foil angles. The configuration ID is the x coordinate in Figure 4.12, L/R and U/D denote the event count ratio between left/right and up/down detector pairs and the angles denote the tilt angle of the foil.

Configuration ID	Configuration	Asymmetry %	Error %
1	L/R $-70°/+70°$	-1.70	1.98
2	U/D $-70°/+70°$	5.62	2.12
3	L/R $-70°/0°$	0.19	3.53
4	U/D $-70°/0°$	5.64	3.99
5	L/R $+70°/0°$	1.89	3.55
6	U/D $+70°/0°$	0.025	4.02

In order to compare a pure baseline measurement to data with oblique foil angles, Equation 2.9 was used. Results are presented in Figure 4.13 with exact values in Table 4.7. With this method, detection efficiencies are not cancelled out, but it is possible to normalize event counts from oblique foil angle measurements according to the asymmetry from $\alpha = 0°$. Results from normalized counts are presented in Figure 4.14.

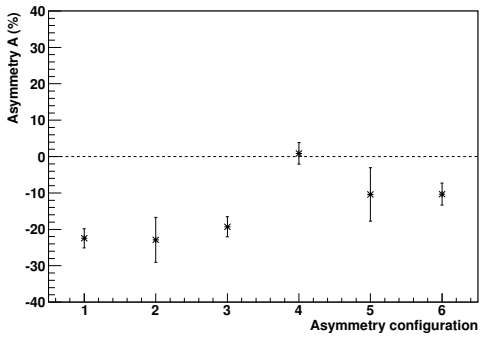

Figure 4.13: Asymmetries calculated for fixed foil angles using Equation 2.9. Exact values and the asymmetry configurations on the horizontal axis can be found in Table 4.7.

Table 4.7: L/R denotes ratio between left and right detector counts and the angles denote the tilt angle of the foil for data in Table 4.4.

Configuration ID	Configuration	Asymmetry %	Error %
1	L/R $-70°$	-22.53	2.61
2	L/R $0°$	-22.89	6.17
3	L/R $+70°$	-19.28	2.74
4	U/D $-70°$	0.88	2.97
5	U/D $0°$	-10.38	7.35
6	U/D $+70°$	-10.33	3.02

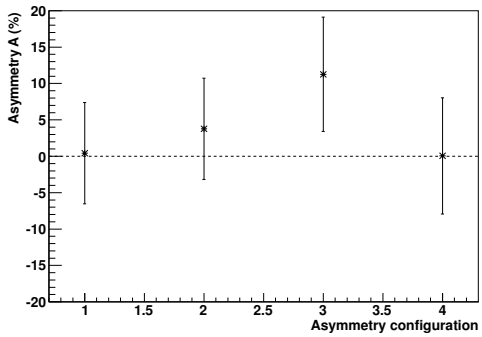

Figure 4.14: Normalized detector count rates based on asymmetry with the foil angle $\alpha = 0°$. Exact values and the asymmetry configurations on the horizontal axis can be found in Table 4.8.

Table 4.8: Normalized asymmetries and errors based on asymmetry from $\alpha = 0°$ for data in Table 4.4.

Configuration ID	Configuration	Asymmetry %	Error %
1	L/R $-70°$	0.39	6.94
2	L/R $+70°$	3.78	6.97
3	U/D $-70°$	11.25	7.85
4	U/D $+70°$	0.051	7.97

As a consistency check over the duration of the experiment, the experimental runs were split into ten parts, or batches, with an equal experimental running time for all batches, giving approximately 120 events in each. The double ratio asymmetry value and statistical error was calculated for each batch. The raw counting rates are presented in Table 4.5 and the weighted mean and error of the data in Table 4.9 with plots in Figure 4.15. The baseline measurements with foil tilt angle $\alpha = 0°$ were not used.

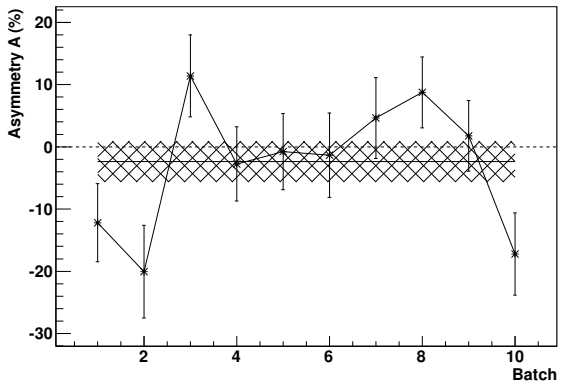

(a) Left-right asymmetry for $\alpha = \pm 70°$.

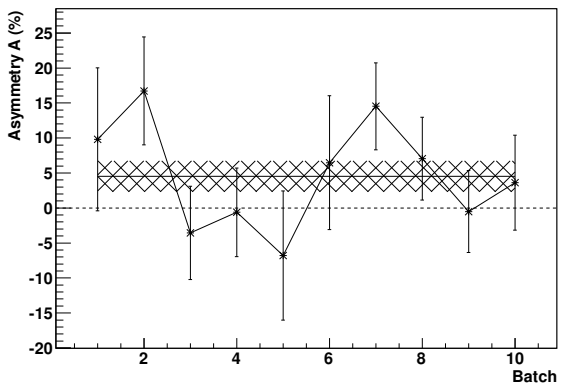

(b) Up-down asymmetry for $\alpha = \pm 70°$.

Figure 4.15: Double ratio scattering asymmetry with exact values in Table 4.9. The solid horizontal line is the weighted mean asymmetry value, the dotted line represents perfect symmetry and the hatched band represents the extent of the error on the weighted mean. The batch number represents the ten chunks that the experimental data was cut into with approximately 120 events in each chunk.

Table 4.9: Weighted mean, error and χ^2 on the asymmetry value for data in Table 4.5. According to the χ^2 measure, the error for L/R $\alpha = \pm 70^\circ$ was severely underestimated and therefore scaled by the reduced χ^2, following the procedure described in [39].

Configuration	Mean	Error	χ^2	$F_{\chi^2}(\eta = 9)$
L/R $\alpha = \pm 70^\circ$	-1.96%	3.19%	23.05	0.99
U/D $\alpha = \pm 70^\circ$	4.52%	2.22%	9.99	0.65

4.6 Discussion of results

If the nuclear spin polarization is the major contributor to particle scattering asymmetry, the asymmetry calculated with the L/R detector pair with a foil angle $\alpha = \pm 70^\circ$ should be non-zero and all other asymmetries should be zero. This is however not the case. In Figure 4.12, in which the double ratio method from Equation 4.3 was used, the asymmetry L/R is consistent with zero asymmetry within one σ. At the same time, the U/D asymmetry is 2.6σ away from zero, with σ similar to L/R asymmetry (due to similar statistics). This means that there is clearly an instrumental asymmetry, which ideally should be taken into account and corrected for. In combination with the $\alpha = 0^\circ$ baseline measurement, the statistical errors are too large to draw any conclusion about measurements with individual foil angles.

The ratio from Equation 2.9, used for Figure 4.13, shows large baseline asymmetries. One possible reason for this is different detection efficiencies of the left and right detectors, which can be resolved by normalizing the event counts for the oblique foil angle measurements, as has been done for Figure 4.14. With polarization, in Figure 4.14 we expect to see an asymmetry in L/R of opposite sign for $\alpha = \pm 70^\circ$. However, within statistical errors, the asymmetry is consistent with zero. Measurements with U/D should be close to zero and they are within 1.5 sigma.

Figure 4.15 presents the time evolution of the asymmetry. Due to the low statistics when dividing the event counts, the errors are rather large and the asymmetries fluctuate. As discussed above, within the statistical errors,

non-zero asymmetry in L/R cannot be concluded.

To summarize, within the statistics that were collected for this experiment, we can not conclude whether we have, or have not, measured an asymmetry in the scattered particles due to a nuclear spin polarization.

The atomic polarization p_J of ^{21}Ne in any of the charge states present after passage through each foil should be around 10–20% as reported from previous experiments. With 3 foils, Equation 2.10 yields a nuclear polarization of $p_I = 0.34 p_J$, and with 20 foils, $p_I = 1.31 p_J$, giving several percent nuclear polarization. Currently, the expression between particle asymmetry and nuclear polarization is not known, but it could be derived from the formal theory presented in the theory section. An alternative approach would be to include spin polarization in the widely-used Coulomb-excitation code GOSIA [24]. The Warsaw group is presently trying to implement this feature in the code, but the project is not yet finalized. In the meantime we tentatively say that the asymmetry can be only smaller or equal to the underlying polarization, thus the observed particle asymmetry would at most amount to several percent. The present result may therefore be consistent with the expected asymmetry, only the statistical uncertainties are too large. Clearly, one way to improve the result would be to decrease the statistical errors and to increase the initial nuclear polarization, possibly by a longer experimental run and by introducing more foils. However, each foil interaction causes energy loss and angular straggling of the beam, so the number of foils was kept at a moderate level for this experiment.

Below we will discuss some problems with the present data, which led to lower than expected statistics and which might have caused some systematic effects. If a new experiment can be scheduled at ISOLDE, these points should be addressed.

As demonstrated in Figure 4.9, there was a problem with the barrel strip length-wise positioning. Above 12 MeV, the resistive layer is not able to provide high enough readout to compensate for the readout of the dE detector. Scattering kinematics and plots show there is a lot of statistics at higher energies that would be lost with an energy cut at 12 MeV. In summary, the

positioning information could not be used consistently for most events.

Due to the lack of positioning information from the barrel strips, Doppler correction could not be performed to the full extent possible with MINIBALL. A broad peak introduces integrated background which in turn reduces the asymmetry value. It is possible to exclude the integrated background, but the error will increase. Assume that $n_i = N_i + e_i$, where n_i is the observed count rate in direction i (left or right), N_i is the count rate from neon events which we are interested in and e_i is the contribution from the background. If efficiency issues can be ignored, the correct asymmetry value is:

$$A = \frac{N_r - N_l}{N_r + N_l} = \frac{(n_r - e_r) - (n_l - e_l)}{(n_r - e_r) + (n_l - e_l)} = \frac{(n_r - n_l) - (e_r - e_l)}{(n_r + n_l) - (e_r + e_l)}$$

The background sum in the denominator is the integral of background events which is trivial to estimate. The background difference in the nominator is not as trivial, but any efficiency or other proportional discrepancies would vanish in a double ratio expression. One possibility to make use of the double ratio is to extract n_l and n_r since we know the ratio and the sum of counts.

$$\begin{aligned} A' &= \frac{1-\rho}{1+\rho} \approx \frac{n_r - n_l}{n_r + n_l} \\ \rho^2 &= \frac{n(\alpha, d_r)n(-\alpha, d_l)}{n(\alpha, d_l)n(-\alpha, d_r)} \\ n &= n_r + n_l \Rightarrow n_r = \frac{n(A'+1)}{2} \\ A &\approx \frac{n_r - n_l}{n - e} = \frac{nA'}{n-e},\ e = e_l + e_r \end{aligned}$$

This will improve the asymmetry value because $n/(n-e) > 1$, but the error will also grow due to the assumption of zero difference in background. At this point, the large deviations in the asymmetry is of greater concern than the magnitude of the asymmetry, so no asymmetry improvements shall be presented.

The measured non-zero baselines were assumed to originate from detection efficiency. It is possible that the beam is not perfectly aligned with the setup,

and as has been mentioned, the foil holder may thus interact with the beam. Because the geometry of the setup changes with the foil angle, it may be that the baseline can not be expressed linearly which was assumed for the analysis of this experiment. To investigate or resolve this issue, the extents of the beam could be measured at the foils position and foils with a larger aperture for the beam may be installed. If the beam does not hit the target in the middle, the angular coverage between the left and right detectors can change slightly. Looking only at the geometrical coverage, the angular coverage of left and right barrel detectors for a Gaussian beam profile in the target changes by 3.5% if the beam center is moved from the center by 2 mm in the horizontal plane along the target surface, and 4 mm yields 6.5%. A point-like beam was integrated numerically from an analytical expression and the Gaussian beam with a simple Monte Carlo simulation, both giving almost the same results. If this effect is not due to scattering on the foil holder, this type of efficiency will vanish in the double ratio. However, full simulation of potential scattering would be interesting.

Chapter 5

Summary and outlook

The first evaluation experiment of tilted foils for nuclear spin polarization with Coulomb excitation as a polarization monitor has been performed at ISOLDE. A beam of stable ^{21}Ne with $A/q = 4.2$ was accelerated in the REX-ISOLDE linac and passed through three carbon foils, each with thickness $4\,\mu g/cm^2$, angled at 70° to the beam, in order to obtain a beam of nuclei with polarized nuclear spin. The beam impinged thereafter on a target of $2.0\,mg/cm^2$ ^{120}Sn. Gamma radiation and scattered particles were detected with the MINIBALL spectrometer and the T-REX barrel detector chamber. The current results show a measured asymmetry that is consistent with zero asymmetry according to statistical analysis, although better statistics may demonstrate an asymmetry of several percent consistent with expectations.

This was the first Coulomb excitation experiment with the T-REX detector setup, so optimal settings were not known. Particle spectra with the two targets ^{60}Ni and ^{120}Sn target showed no clear structures expected from reaction kinematics, probably due to the strong energy spread in the reaction target affecting the recoiling ions. However, with the lower threshold of 6 MeV applied on the particle energy, a large quantity of noise could be removed in the related gamma spectra. The length-wise coordinates in the resistive strips in the T-REX detectors could not be reconstructed due to saturated energy read-

outs, which reduced the effeciency of the Doppler correction and broadened the particle kinematics spectra which forced high tolerance gates on events. Total collected statistics were rather low and since the beam current was already rather high for the T-REX setup, the only way of improvement would be with a longer experimental or with higher detection efficiency and solid angle coverage. The beam energy was not optimal for tilted foils according to earlier experiments which suggest beam energies in the order of 100 keV/u. This must be taken into consideration together with Coulomb excitation cross section, that drops rapidly for lower velocities, however.

Currently, the analysis can not prevent a large amount of background events from being included in the calculation of the asymmetry value, due to the wide gamma gate to fully cover the Doppler broadened gamma peak and the conservative particle gates. This increases the signal-to-noise ratio for a reduced asymmetry value, but it does no destroy the value.

Before attempting a potential future experiment to improve the results, the above mentioned issues must be addressed. It would be interesting to look at an experiment designed specifically to evaluate the barrel detector response for medium or heavy nuclei from scattering reactions. Clear kinematics curves in the $E(\theta)$ plots and better strip length-wise positional information would improve event selection, but also verify the data collected in the experiment. A thin target will reduce the residue particle energy uncertainty, but also reduce the Coulomb excitation cross section. Finally, the beam interaction with the foil holder should be investigated to rule out systematic errors due to geometric changes in the setup.

An alternative method of measuring nuclear spin polarization is the β-NMR technique. This is actively utilized at ISOLDE with low-energy beams, but there was no such setup installed after the REX-ISOLDE linac at the start of this evaluation project. It also requires a β-active beam with a half life in the order of a second or less. The construction and commissioning of such a device constitutes parts of this project but is outside the scope of this thesis.

Glossary

CGC Clebsch-Gordan coefficients.

CLX Coulomb excitation cross section calculation program provided for MINIBALL experiments.

GOSIA Comprehensive suite of Coulomb excitation analysis source code.

HPGe High Purity Germanium, a common crystalline material for detectors with very high purity.

linac Linear accelerator.

ISOLDE ISotope OnLine separator DEvice, experimental facility at CERN capable of producing a wide range of exotic radioactive isotopes.

MARaBOU MBS And ROOT Based Online/Offline Utility, MBS and ROOT.

MINIBALL Gamma spectrometer after the REX-ISOLDE linear accelerator used for Coulomb excitation and transfer reaction experiments.

MBS Multi Branch System, data acquisition system developed at GSI.

REX Radioactive beam EXperiment at ISOLDE, linac delivering beams with $2.5 < A/q < 4.2$ and $0.3\,\mathrm{MeV/u} < E_{beam} < 3\,\mathrm{MeV/u}$.

ROOT [40] Object Oriented data analysis software developed at CERN.

T-REX Segmented particle detector setup designed for detecting light ejectile particles in transfer reaction exteriments at MINIBALL.

XIA DGF 4C XIA Digital Gamma Finder, digital sampling module used at MINIBALL to acquire data from the HPGe detectors.

Acknowledgments

I would like to express my gratitude to the following group of people who have made the experiment possible and a remarkable learning experience.

Georgi Georgiev, for starting up the project and contributing with a lot of insight into nuclear physics and especially into nuclear structure studies and experimental methods.

Magdalena Kowalska for eagerly offering help during the analysis and for the thorough and, from her point of view, untimely scrutiny of this thesis.

Thomas Nilsson for interesting discussions to bring light into the analysis when all hope seemed lost.

Christophe Sotty, a Ph.D. student in the same project of evaluating tilted foils polarization at ISOLDE. Together, we spent many hours (through many nights) collecting and deciphering data from experiments and real life.

Fredrik Wenander for his dedication to his work and for always being available for discussions of any nature, mostly in physics, of course.

Jarno Van de Walle for helping with preparing the experiment and for valuable insight into signatures and issues with Coulomb excitation during the analysis.

Alexander Herlert and Yorick Blumenfeld for the occasional physics input and for making sure my administrative obligations did no remain in limbo.

Magnus Eriksson for the design, manufacturing and installation of the tilted foils device, and for collaborative calibration and nerve wrecking loading of the thin foils.

Janne Pakarinen for participating in the experiment and for educating me in the many details of physics experiments at the MINIBALL setup.

Kathrin Wimmer for guidance in the analysis especially of the T-REX chamber, including the analysis framework and programs.

Jan Diriken, Nigel Warr and Michael Seidlitz for their assistance and input in positional calibration of gamma detectors.

And like the icing on the cake, my family for all the support and help so I could get where I am with as few mishaps as possible, and my friends for the fun and games after work.

Bibliography

[1] Georgiev G, Hass M, Herlert A, Balabanski D L, Fiori E, Gustafsson A, Hemmingsen L, Imielski P and Johnston K. Geneva: CERN; 2009 Jan. 4 p. CERN-INTC-2009-015 ; INTC-I-083.

[2] Kugler E. The ISOLDE facility. Hyp. Int. 2000 Dec; 129:23–42.

[3] The ISOLDE facility [Internet]. Geneva: CERN; 2012 [cited 2012 Feb 3]. Available from: http://isolde.web.cern.ch/.

[4] Van Duppen P and Riisager K. Physics with REX-ISOLDE: from experiment to facility. J. Phys. G 2011 Jan 11; 38(2):024005, 24 p.

[5] Keim M, Georg U, Klein A, Neugart R, Neuroth M, Wilbert S, Lievens P, Vermeeren L, Brown B A and the ISOLDE Collaboration. Measurement of the electric quadrupole moments of $^{26-29}$Na. Eur. Phys. J. A 2000; 8(1):31–40.

[6] Eder R, Berkers I, Brown D E, Grand I S, Hagn E, Harding P, Hassani R, Herzog P, Kastelein B, Knipper A, Marguier G, Massaq Q, Ohya S, Postma H, Prinz J, Richard-Serre C, Romanski I, Schlösser K, Stone N J, Vanderpoorten W, Vanhaverbeke J, Vanneste L, Wölfle T, Zech E and the ISOLDE collaboration. Nicole: New on-line orientation facility at ISOLDE/CERN. Hyp. Int. 1990; 59(1–4):83–90.

[7] Wenander F. Charge breeding of radioactive ions with EBIS and EBIT. J. Instr. 2010 Oct 21; 5:C10004.

[8] Schmidt P, Ames F, Bollen G, Forstner O, Huber G, Oinonen M, Zimmer J and the REX-ISOLDE collaboration. Bunching and cooling of radioactive ions with REXTRAP. Nucl. Phys. A 2002 Apr 22; 701(1–4):550-556.

[9] Wenander F. EBIS as charge breeder for radioactive ion beam accelerators. Nucl. Phys. A 2002 Apr 22; 701(1–4):528–536.

[10] Habs D, Kester O, Sieber T, Bongers H, Emhofer S, Reiter P, Thirolf P G, Bollen G, Aystö J, Forstner O, Ravn H, Nilsson T, Oinonen M, Simon H, Cederkall J, Ames F, Schmidt P, Huber G, Liljeby L, Skeppstedt O, Rensfelt K G, Wenander F, Jonson B, Nyman G, von Hahn R, Podlech H, Repnow R, Gund C, Schwalm D, Schempp A, Kühnel K U, Welsch C, Ratzinger U, Walter G, Huck A, Kruglov K, Huyse M, Van den Bergh P, Van Duppen P, Weissman L, Shotter A C, Ostrowski A N, Davinson T, Woods P J, Cub J, Richter A, Schrieder G and the REX-ISOLDE Collaboration. The REX-ISOLDE project. Hyp. Int. 2000; 129(1–4):43–66.

[11] Simonius M. Theory of polarization measurements. Observables, amplitudes and symmetries. Lect. Not. Phys. 1974; 30:38–87.

[12] Zupranski P, Dreves W, Egelhof P, Steffens E, Fick D and Rösel F 1979 *Nucl. Instr. Meth.* vol. **167** 193–200

[13] Fano U and Macek J H. Impact Excitation and Polarization of the Emitted Light. Rev. Mod. Phys. 1973 Oct; 45(4):553–573.

[14] Ellis D G. Density-operator description of foil-excited atomic beams: Zero-field quantum beats in L-S coupling without cascades. J. Opt. Soc. Am. 1973 Oct; 63(10):1232–1235.

[15] Andrä H J. Orientation of Atoms by Beam-solid Surface Interaction. Phys. Lett. 1974 Sep 22; 54A(4):315–316.

[16] Winther H and Andra H J. Hyperfine Interaction Using Grazind Beams. Hyp. Int. 1985; 24–26:277–299.

[17] Momota S, Nojiri Y, Fukuda M, Matsuta K and Minamisono T. Mechanism of Polarization Production by Means of the Tilted-Foil Technique Studied Using Beta-Radioactive Nuclei. Hyp. Int. 2002; 142:513–548.

[18] Schröder H and Kupfer E. Model for the Production of Circular Polarization via Beam-Foil Interaction. Z. Phys. A 1976; 279:13–16.

[19] Burgdörfer J, Gabriel H and Schröder H. Theory of Optical Polarization Due to Electron Capture from Localized Target States by Fast Ions. Z. Phys. A 1980; 295:7–16.

[20] Berry H G and Hass M. Beam-Foil Spectroscopy. Ann. Rev. Nucl. Part. Sci. 1982; 32:1–34.

[21] Goldring G and Niv Y. Nuclear Polarization Generated in Multi Tilted-Foil Arrays. Hyp. Int. 1985; 21:209–218.

[22] Berry H G, Bhardwaj S N, Custir L J and Schectman R M. Orientation and Alignment of Atoms by Beam Foil Interaction. Phys. Lett. 1974 Nov 4; 50A(1):59–60.

[23] Bendahán J, Broude C, Hass M, Dafni E, Goldring G, Gerl J, Habs D, Korten W and Schwalm D. Heavy Ion Beam Polarization Produced by the Multi-Tilted-Foil Interaction. Z. Phys. A 1988; 331:343–346.

[24] Cline D, Czosnyka T, Hayes A B, Napiorkowski P, Warr N and Wu C Y. GOSIA User Manual for Simulation and Analysis of Coulomb Excitation Experiments. [Internet] 2012 Jan 25 [cited 2012 Feb 21]. Available from: http://www.pas.rochester.edu/ cline/Gosia/Gosia_Manual_20120125.pdf

[25] ISOLDE yields database [Internet]. Geneva, CERN. [cited 2012 Feb 25]. Available from: https://oraweb.cern.ch/pls/isolde/query_tgt

[26] Evaluated Nuclear Structure Data File (ENSDF) [Internet]. Brookhaven National Laboratory. [cited 2012 Feb 25]. Available from: http://www.nndc.bnl.gov/ensdf/

[27] Eriksson M. Installation of Mobile Tilted Foils Holder at REX-ISOLDE. Geneva; CERN. 2010 [cited 2012 Feb 25] Available from: https://espace.cern.ch/be-dep/OP/ISOLDE/Documents/Documentation/REX/Installation

[28] Van de Walle J. The Miniball at REX-ISOLDE. 2011; to be submitted to EPJ.

[29] Bildstein V, Gernhäuser R, Kröll T, Krücken R, Raabe R, Van Duppen P, REX-ISOLDE and MINIBALL Collaborations. A new setup for transfer reactions at REX-ISOLDE. Prog. Part. Nucl. Phys. 2007; 59:386–388.

[30] XIA DGF-4C [Internet]. Hayward, CA: XIA LLC c2012 [updated 2012 Jan 23; cited 2012 Feb 2]. Available from: http://www.xia.com/DGF-4C.html

[31] Warr N and Seidlitz M. Personal communications. 2010.

[32] MARaBOU [Internet, cited on 2012 Feb 25]. Available from: http://www.bl.physik.tu-muenchen.de/marabou/html/

[33] MBS [Internet, cited on 2012 Feb 25]. Available from: http://www-win.gsi.de/daq/

[34] Miniball electronics at May 2009 [Internet, cited on 2012 Feb 25]. Available from: http://www.ikp.uni-koeln.de/ warr/doc/electronics_May2009.pdf

[35] Wimmer K, Krücken R, Bildstein V, Faestermann T, n Gernhäuser R, Habs D, Thirolf P, Lutter R, Csige L, Van Duppen P, Raabe R, Patronis N, Bree N, Huyse M, Elseviers J, Diriken J, Van de Walle J, Pakarinen J, Clement E, Cederkäll J, Voulot D, Stora T, Wenander F, Fraile L M, Davinson T, Woods P J, Nilsson T, Tengborn E, Chapman R, Smith J F, Angus L, Labiche M, Wady P, Jenkins D, Butterworth J, Nara Singh B S, Freeman S, Fitzpatrick C, Deacon A, Butler P, Scheck M, Blazhev A, Warr N, Reiter P, Seidlitz M, Georgiev G, Fiori E, Lozeva R, Kröll

T, Pietralla H, Schrieder G, Balabanski D, Lo Bianco G, Das Gupta S, Nardelli S, Görgen A, Korten W, Obertelli A, Hadynska-Klek K, Iwanicki J, Napiorkowski P J, Srebrny J, Wrzosek-Lipska K, Zielińska M, and the REX-ISOLDE and MINIBALL collaborations. Study of the onset of deformation and shape coexistence in ^{46}Ar via the inverse kinematics (t,p) reaction. Proposal to the INTC committee 2009 Oct 14. CERN-INTC-2009-034 / INTC-P-270.

[36] Wimmer K. Discovery of the shape coexisting 0^+ state in ^{32}Mg [PhD thesis]. Technische Universität München Physik-Department E12; 2010.

[37] Simulation of fragment separators [Internet, cited on 2012 Feb 25]. Available from: http://groups.nscl.msu.edu/lise/lise.html

[38] Ower H. [PhD. thesis]. Universität Frankfurt; 1980.

[39] Eidelman S. Review of Particle Physics. Phys. Lett. B 2004 July 15; 592:1.

[40] Brun R and Fons R. ROOT - An object oriented data analysis framework. Nucl. Instr. Meth. Phys. Res. A 1997; 389(1–2):81–86.